

The SLUGGS survey: combining stars, globular clusters and planetary nebulae to understand the assembly history of early-type galaxies from their large radii kinematics

Arianna Dolfi,^{1*} Duncan A. Forbes,¹ Warrick J. Couch,¹ Kenji Bekki,³ Anna Ferré-Mateu,^{2,1}
Aaron J. Romanowsky,^{4,5} Jean P. Brodie,^{1,5}

¹ Centre for Astrophysics & Supercomputing, Swinburne University of Technology, Hawthorn VIC 3122, Australia

² Institut de Ciències del Cosmos (ICCUB), Universitat de Barcelona (IEEC-UB), E02028 Barcelona, Spain

³ ICRAR, M468, The University of Western Australia 35 Stirling Highway, Crawley Western Australia, 6009, Australia

⁴ Department of Physics & Astronomy, San José State University, One Washington Square, San Jose, CA 95192, USA

⁵ University of California Observatories, 1156 High St., Santa Cruz, CA 95064, USA

Accepted 2021 April 09. Received 2021 March 29; in original form 2021 February 01

ABSTRACT

We investigate the kinematic properties of nine nearby early-type galaxies with evidence of a disk-like component. Three of these galaxies are located in the field, five in the group and only one in the cluster environment. By combining the kinematics of the stars with those of the globular clusters (GCs) and planetary nebulae (PNe), we probe the outer regions of our galaxies out to $\sim 4\text{--}6R_e$. Six galaxies have PNe and red GCs that show good kinematic alignment with the stars, whose rotation occurs along the photometric major-axis of the galaxies, suggesting that both the PNe and red GCs are good tracers of the underlying stellar population beyond that traced by the stars. Additionally, the blue GCs also show rotation that is overall consistent with that of the red GCs in these six galaxies. The remaining three galaxies show kinematic twists and misalignment of the PNe and GCs with respect to the underlying stars, suggesting recent galaxy interactions. From the comparison with simulations, we propose that all six *aligned* galaxies that show similar dispersion-dominated kinematics at large radii ($> 2\text{--}3R_e$) had similar late ($z \lesssim 1$) assembly histories characterised by mini mergers (mass-ratio $< 1:10$). The different V_{rot}/σ profiles are then the result of an early ($z > 1$) minor merger ($1:10 < \text{mass-ratio} < 1:4$) for the four galaxies with *peaked and decreasing* V_{rot}/σ profiles and of a late minor merger for the two galaxies with *flat* V_{rot}/σ profiles. The three *mis-aligned* galaxies likely formed through multiple late minor mergers that enhanced their velocity dispersion at all radii, or a late major merger that spun-up both the GC sub-populations at large radii. Therefore, lenticular galaxies can have complex merger histories that shape their characteristic kinematic profile shapes.

Key words: galaxies: elliptical and lenticular, cD – galaxies: formation – galaxies: kinematics and dynamics – galaxies: star clusters: general – planetary nebulae: general

1 INTRODUCTION

Early-type galaxies (ETGs; i.e. elliptical and lenticular) are found to be more numerous towards the denser regions of rich galaxy clusters (Dressler 1980), with the fraction of lenticular (S0) galaxies increasing by a factor of 2–3 in such regions between $z \simeq 0.5$ and the present day at the expenses of spirals (Dressler et al. 1997; Fasano et al. 2000). This suggests that S0 galaxies could be formed from spirals with quenched star formation and faded spiral arms, as a result of cluster-related physical processes, such as ram-pressure stripping, tidal interactions and starvation, that stripped the gas envelope sur-

rounding the spiral galaxy or suppressed its gas supply from the Intergalactic Medium (IGM) (e.g. Gunn & Gott 1972; Larson et al. 1980; Bekki 2009; Bekki & Couch 2011; Mersuzi et al. 2016).

However, all these physical processes require a high density environment in order to be most effective. The observations of S0s in low-density environments, where the interactions between galaxies are limited or non-existent, require alternative formation pathways. Mergers and accretion events have been shown to be able to produce S0 galaxies (e.g. Bekki 1998; Bournaud et al. 2005; Naab et al. 2014; Tapia et al. 2017; Eliche-Moral et al. 2018). Specifically, Bournaud et al. (2005) showed that minor mergers with mass-ratio 1:4.5–1:10 can produce disk ETGs, resembling the kinematics and mor-

* E-mail: adolfi@swin.edu.au

phology of S0s, while major mergers with mass-ratio 1:1-1:3 are likely to produce elliptical (E) galaxies with hotter kinematics. However, [Tapia et al. \(2017\)](#) and [Eliche-Moral et al. \(2018\)](#) have shown that a few Gyrs after a major merger, many galaxy remnants displayed relaxed morphology and properties typical of S0s, suggesting that major mergers are also a possible S0 formation pathway.

Alternatively, a secular evolution scenario has been proposed for the formation of S0 galaxies, where the spiral galaxy evolves mostly passively, consuming its own in-situ gas through star formation, and slowly fades due to internal processes and instabilities. This scenario is expected to produce more rotationally-supported S0s, as they preserve a higher degree of rotation of their progenitor spiral. Internal processes, such as the collapse of a cold disk that becomes gravitationally unstable at high redshifts, feedback events from active galactic nuclei (AGN) and quenching of star formation due to the stabilization of the gas disk (i.e. morphological quenching), have been proposed as possible formation pathways for S0 galaxies ([Martig et al. 2009](#); [Saha & Cortesi 2018](#); [Mishra et al. 2018](#)). [Bellstedt et al. \(2017\)](#) and [Rizzo et al. \(2018\)](#) have found S0 galaxies displaying high values of stellar angular momentum, which are more consistent with those of disk galaxies rather than with those of merger remnants.

Finally, an alternative scenario involves the build-up of a disk component around a massive compact quiescent galaxy at high redshift ([Damjanov et al. 2014](#)) from the accretion of a gas-rich dwarf galaxy ([Diaz et al. 2018](#)).

Many physical processes have been thus shown to be able to produce S0 galaxies, therefore a wide range of stellar kinematic and population properties should be expected in S0s formed through these different formation pathways, as well as in the different environments.

Early results from the ATLAS^{3D} survey ([Cappellari et al. 2011](#)) classified a sample of 260 nearby ETGs (i.e. S0s and Es) into the two families of fast and slow rotators, based on the stellar kinematics of the central $1R_e$ ([Emsellem et al. 2011](#)). The fast rotators typically showed regular rotation patterns with aligned kinematic and photometric position angles, while the slow rotators showed more complex velocity fields with misaligned kinematic and photometric position angles and were typically found among the most massive galaxies and in higher density environments. These results suggested a wide range of different processes for the formation of the fast/slowly rotating ETGs (e.g. mergers, interactions, gas stripping and secular evolution; [Krajnović et al. 2011](#)).

[Coccato et al. \(2020\)](#) studied the stellar kinematics out to $\sim 1.5-2R_e$ for a sample of 21 S0 galaxies located in field and cluster environments. Their results showed that cluster S0s were more rotationally supported (i.e. high V_{rot}/σ) and consistent with a faded spiral scenario, while field S0s were more pressure supported (i.e. low V_{rot}/σ) and consistent with a formation through minor mergers. They also performed a stellar population analysis of such S0s, but they did not find any clear environmental dependence as for the stellar kinematics. However, the subsequent work by [Johnston et al. \(2020\)](#), that specifically focused on the stellar population analysis of 8 of the S0s from [Coccato et al. \(2020\)](#), found that the field S0s had a younger stellar population than the cluster S0s, therefore suggesting a minor merger formation pathway. Similar conclusions to [Coccato et al. \(2020\)](#) were reached by [Deeley et al. \(2020\)](#), who studied the stellar and gas kinematics of

a sample of 219 S0 galaxies from the SAMI survey ([Croom et al. 2012](#)). [Deeley et al. \(2020\)](#) found that pressure supported S0s were located in low-density environments (i.e. field and small groups) and had misaligned stellar and gas kinematics, consistent with a minor merger formation scenario. On the other hand, rotationally supported S0s were located in high-density environments and had kinematic properties more similar to spiral galaxies, therefore suggesting a faded spiral formation scenario. [Tous et al. \(2020\)](#) have identified two sub-populations of S0s, one being characterized by S0s with star formation rates similar to those of late-type spirals and the other being characterized by quiescent S0s. They find that the sub-population of active S0s is slightly less massive with a younger and more metal-poor stellar population than the quiescent S0s, and is predominantly located in low-density regions ([Tous et al. 2020](#)), suggesting that the environment has likely played some role in the formation of S0s.

[Fraser-McKelvie et al. \(2018\)](#) suggested that the stellar mass of the galaxies, rather than the environment, is the main discriminator in the formation of S0s from the stellar population analysis of a sample of S0 galaxies in the MaNGA survey ([Bundy et al. 2015](#)). Specifically, [Fraser-McKelvie et al. \(2018\)](#) found that more massive S0s had an older and more metal-rich stellar population in the bulge than in the disk, while low-mass S0s had a younger stellar population in the bulge than in the disk, suggesting an inside-out quenching scenario for the more massive S0s and an outside-in quenching scenario for the low-mass S0s. A more recent stellar population analysis of a sample of S0 galaxies in the MaNGA survey has also revealed a bimodal S0 population, with massive S0s (i.e. $M_* > 3 \times 10^{10} M_\odot$) having mostly flat metallicity gradients and low-mass S0s having steeper metallicity gradients, while the age gradients show the opposite trend ([Domínguez Sánchez et al. 2020](#)). These results suggest that gas-rich mergers are more important in the formation of massive S0s.

The SAGES Legacy Unifying Globulars and GalaxieS (SLUGGS; [Brodie et al. 2014](#)) survey was able to obtain extended stellar kinematic measurements out to $\sim 2-4R_e$ for a sample of 25 nearby ETGs (including S0s), as well as radial velocities for a large number of globular clusters (GCs; [Forbes et al. 2017a](#)). From the stellar kinematics, [Arnold et al. \(2014\)](#) and [Foster et al. \(2016\)](#) found that the kinematic behaviour of the central $1R_e$ of ETGs can be quite different from the kinematic behaviour of the outer galaxy regions, with centrally fast rotators often showing decreasing or rapidly increasing rotation at larger radii. Specifically, [Arnold et al. \(2014\)](#) found that many of their ETGs showed evidence of a fast-rotating stellar disk embedded in a more slowly rotating spheroidal component, which is consistent with the model of a two-phase formation scenario (e.g. [Oser et al. 2010](#); [Zolotov et al. 2015](#); [Rodríguez-Gomez et al. 2016](#)). According to the two-phase model, massive ETGs formed at early times (i.e. $z \geq 2$) with a rapid collapse or wet merger event during which they formed most of their stellar mass, in a compact object known as 'red-nugget' ([Damjanov et al. 2014](#); [Zolotov et al. 2015](#)), i.e. in-situ formation. At later times (i.e. $z \simeq 0$), they mostly grew in size through the accretion of low-mass dwarf galaxies deposited onto their outskirts (ex-situ formation). These low-mass mergers are responsible for producing the decreasing rotation in the outer regions of ETGs. However, stellar kinematic studies of different samples of ETGs, extending beyond $2R_e$, found different results from [Arnold](#)

et al. (2014), with centrally fast rotator galaxies remaining fast-rotating and centrally slow rotator galaxies remaining slow-rotating beyond $1R_e$ (Raskutti et al. 2014; Boardman et al. 2017). The differences between these works could be due to differences in the sample selection criteria. For instance, the sample of ETGs from Boardman et al. (2017) contains ETGs with lower stellar masses than the SLUGGS sample, therefore the transition radius (which anti-correlates with the galaxy stellar mass; Pulsoni et al. 2020) in the stellar kinematics of the galaxies from Boardman et al. (2017) could simply be located at larger radii as compared to the SLUGGS galaxies. Nevertheless, all these results suggest the importance of studying the kinematic properties of larger samples of ETGs out to larger radii. This will not only help us to constrain the formation histories of ETGs, but also to understand the kinematic behaviour of the galaxy outskirts with respect to that of the galaxy central regions.

The stellar kinematic results obtained by Arnold et al. (2014) and Foster et al. (2016), as part of SLUGGS, have shown the importance of studying the kinematic properties of the outer regions of ETGs, i.e. beyond $\sim 2-3R_e$. In fact, the galaxy outskirts are characterized by longer dynamical timescales, therefore they better preserve the imprints of the galaxy formation processes in the stellar dynamic and population content. However, the galaxy outskirts are difficult and time-consuming to observe due to their lower surface brightness as compared to the inner regions.

One way to overcome this issue and probe the outskirts of the galaxies is to use discrete kinematic tracers, such as GCs and planetary nebulae (PNe). GCs are observed in all galaxy types and numerous in the most massive ETGs. They are typically found to display a colour bimodality that reflects the two distinct sub-populations of the red, metal-rich and blue, metal-poor GCs, which are expected to trace the kinematic properties of the host ETGs differently (Forbes et al. 1997; Strader et al. 2005; Brodie & Strader 2006). Specifically, the red, metal-rich GCs are expected to have formed largely in-situ together with the bulk of the host galaxy stars, while the blue, metal-poor GCs are expected to have formed mostly at early times of the galaxy formation process or subsequently accreted onto the host galaxy from tidally stripped dwarfs during the late evolutionary phase of the galaxy. Therefore, the red, metal-rich GCs should trace the kinematic properties of the stellar population of the bulge and spheroid in massive ETGs, while the blue, metal-poor GCs have typically a more extended spatial distribution than the red GCs and should trace the kinematic properties of the stellar population of the galaxy halo (Forbes et al. 1997; Forbes & Remus 2018). PNe are a late evolutionary stage of the stars with stellar masses $1M_\odot < M^* < 8M_\odot$ and are expected to trace the underlying stellar population in ETGs out to large radii (e.g. Romanowsky 2006; Buzzoni et al. 2006).

Since GCs are bright star clusters and PNe are strong [OIII] emitters, they can be observed out to larger radii (i.e. $\sim 8-10R_e$) in ETGs, where the stellar component becomes too faint for spectroscopy studies. Some previous works have found that the PNe and GCs are generally good tracers of the kinematics of the underlying stellar population and stellar surface brightness profile for many ETGs (e.g. Coccato et al. 2009; Pota et al. 2013, 2015). Others adopted a novel approach to study the formation histories of S0 galaxies that combined the kinematics of the PNe and GCs with the photo-

metric decomposition (i.e. bulge+disk) of the galaxy in order to associate the PNe and GCs to either the bulge or disk component using a maximum likelihood method (e.g. Cortesi et al. 2011; Forbes et al. 2012; Cortesi et al. 2013a, 2016; Zanatta et al. 2018).

Recent simulations extending out to large galactocentric radii, i.e. $5R_e$ (Schulze et al. 2020), have shown that different V_{rot}/σ profiles can be the result of merger events that occurred at different redshifts. These merger events are expected to influence not only the kinematics of the stars, but also that of both GC sub-populations depending on the mass-ratio and orbital configuration of the mergers (Bekki et al. 2005; Cavanagh & Bekki 2020). Therefore, in this work, we study the kinematic profiles for a sample of 8 selected S0 and E/S0 galaxies in the SLUGGS survey that are located mainly in low-density environments by combining the stellar with the GC and PNe kinematics in order to reach beyond $\sim 2-3R_e$, similarly to what has already been done in Dolfi et al. (2020) for the nearest S0 galaxy, NGC 3115. If the PNe and GCs are tracing the kinematics of the underlying stellar population in the galaxies, then we can use them as proxies for the stars to study the galaxy outskirts beyond the radius probed by the stars. From the comparison of the overall V_{rot}/σ kinematic profiles of the galaxies out to large radii, i.e. $\sim 5R_e$, with the simulations, we can constrain the merger history of our galaxies with the most likely epoch when the merger event occurred that shaped the characteristic V_{rot}/σ profiles of our galaxies.

The structure of the paper is as follows. In Sec. 2, we describe the selected sample of ETGs with their stellar, GC and PNe kinematic data. In Sec. 3, we present the kinematic results in the form of 2D kinematic maps and 1D kinematic profiles for all the kinematic tracers of each individual galaxy. In Sec. 4, we discuss the likely formation histories of our sample of S0 galaxies from the comparison with simulations of galaxy formation. Appendix A gives a more detailed description of the kinematic properties of each one of our individual selected ETGs.

2 THE GALAXY SAMPLE

We select a sample of 8 ETGs out of 25 from the SLUGGS survey (Brodie et al. 2014), based on the availability of a sufficient number of both GCs and PNe with measured radial velocities in order to study their kinematic properties. The GC and PNe spectroscopic catalogues come from the SLUGGS (Forbes et al. 2017a) and the extended Planetary Nebula Spectrograph (ePN.S; Pulsoni et al. 2018) surveys, respectively. Photometry measurements are available for the GC systems of each one of our selected galaxies and they have been presented in Pota et al. (2013, 2015).

Table 1 shows the list of the 8 selected ETGs with a summary of some of their main characteristics. We also indicate the total number of spectroscopically confirmed GCs and PNe in each galaxy with the adopted colour-split to separate between the red, metal-rich and blue, metal-poor GC sub-populations, where applicable. The colour-splits to separate between the red and blue GCs were selected after visually inspecting the colour-magnitude diagrams, in the corresponding magnitude bands, of the photometric GC catalogues. We note that the GC colour-splits adopted in this work are con-

sistent with those from Pota et al. (2013, 2015) and Cortesi et al. (2016). NGC 3115 is also included in the list, but its study has been carried out in a separate paper (Dolfi et al. 2020). All selected ETGs have a total number of spectroscopically confirmed GCs or PNe greater than 100 and Fig. 1 shows the measured radial velocities of the GC and PNe systems as a function of the galactocentric radius, R/R_e , for each galaxy.

The stellar kinematics for all our galaxies come from ATLAS^{3D} (Cappellari et al. 2011), MUSE (Gu  rou et al. 2016) in the case of NGC 3115, and SLUGGS (Arnold et al. 2014; Foster et al. 2016) surveys. The former provides spatially resolved 2D maps of the inner $1R_e$ of ETGs, while the latter provides discrete stellar kinematic measurements around the galaxies that are obtained using the Stellar Kinematics from Multiple Slits (SKiMS) technique (Proctor et al. 2009; Foster et al. 2009, 2011) and extend further out to $\sim 2-4R_e$. We note here that all our selected ETGs, except for NGC 3115 and NGC 5846, show regular rotation in the 2D kinematic maps of their velocity fields within the central $\sim 1R_e$ and are, thus, classified as fast rotators (Emsellem et al. 2004). NGC 5846 is the only massive ETG in our selected sample classified as slow-rotator within the central $\sim 1R_e$ from ATLAS^{3D} (Emsellem et al. 2004). Finally, NGC 3115 was not observed as part of the ATLAS^{3D} (Cappellari et al. 2011), however the stellar kinematic results from MUSE, extending out to $\sim 3R_e$, show that NGC 3115 is also a fast rotator S0 galaxy (Gu  rou et al. 2016).

We note that 5 out of 9 of our selected ETGs in Table 1 are found in groups, while 3 are found in the field and only one galaxy, NGC 4649, is in a cluster environment. Additionally, we note that only three of the ETGs in Table 1 are classified as pure S0s (i.e. NGC 1023, NGC 3115 and NGC 7457), while the remaining six ETGs are classified as E/S0s or Es. However, even though these six ETGs are not classified as pure S0s based on their morphology (see Table 1), they have been all found to show evidence of a disk-like component from early kinematic or photometric studies (see Appendix A also for more specific details about the main properties of each individual galaxy in Table 1 with the description of their GC and PNe systems).

3 RESULTS

3.1 2D Kinematic maps and 1D kinematic profiles

In this section, we produce the 2D kinematic maps of the GC and PNe tracers, as well as stars, for each galaxy in Table 1. Similarly to Dolfi et al. (2020) and in previous literature works (e.g. Proctor et al. 2009; Foster et al. 2013, 2016; Bellstedt et al. 2017), we use the kriging spatial interpolation technique (Pastorello et al. 2014), which is an inverse-noise-weighted method, to generate the continuous 2D velocity and velocity dispersion maps shown in Fig. 2 and A1-A8. We fold the PNe kinematic catalogue only for NGC 4649 prior to producing the 2D maps in order to have full position angle (PA) coverage around the galaxy, as described in Sec. A2.2.

To estimate the velocity dispersion of the GC and PNe tracers of each galaxy, we calculate the standard deviation of the tracer velocities from the mean in spatial bins centered at the position of each tracer and containing a chosen number

of nearest-neighbour objects. In general, the higher is the number of nearest-neighbour objects, the more accurate the estimate of the velocity dispersion of the GCs and PNe would be in each spatial bin. However, we need to be careful when choosing the number of nearest-neighbour objects so that we do not average together GC and PNe tracers that are located in significantly different spatial regions around the galaxy. For this reason, we use 5 nearest-neighbours for the GCs and 10 nearest-neighbours for the PNe, since the latter have better sampled velocity fields, i.e. higher number of objects in the catalogues. We use 10 nearest-neighbour for the GCs for only NGC 4649 as this galaxy has the largest spectroscopic GC catalogue (see Table 1). This procedure is the same as the one adopted in Dolfi et al. (2020) and it is not necessary for the stellar kinematics for which we have the integrated line-of-sight velocity dispersion.

We calculate the 1D kinematic profiles of all our kinematic datasets, i.e. ATLAS^{3D} and SLUGGS stars, GCs and PNe (see Sec. 2) using the *kinemetry*¹ method (Krajnovi   et al. 2006), which was initially used with 2D spatially resolved stellar kinematic maps of galaxies to recover the best-fitting moments of the Line-Of-Sight-Velocity-Distribution (LOSVD) as a function of the galactocentric radius (e.g. Krajnovi   et al. 2011). Here, we adopt a similar procedure as in Proctor et al. (2009); Foster et al. (2011, 2016); Bellstedt et al. (2017); Dolfi et al. (2020) to recover the LOSVD moments for our non-homogeneous and sparse kinematic datasets, i.e. SLUGGS stars, GCs and PNe. As for the 2D kinematic maps, we use the folded PNe catalogue of NGC 4649 (see Sec. A2.2) to derive its 1D kinematic profiles. Within *kinemetry*, the computation of the best-fitting moments of the LOSVD is performed at the different galactocentric radii by least-squares minimization of the cosine model function, described in equations 3 and 4 of Dolfi et al. (2020), fitted to the observed kinematic data binned in concentric elliptical annuli. For a more detailed description of how we apply *kinemetry* to our kinematic datasets see section 6.2 in Dolfi et al. (2020), while for the equations describing in details the chi-squared minimization procedure within *kinemetry* for recovering the best-fitting LOSVD moments of our kinematic data see Foster et al. (2011, 2016).

As previously done in Dolfi et al. (2020) for NGC 3115, we focus on recovering the first and second order moments of the LOSVD (i.e. V_{rot} and σ , respectively) for all the kinematic datasets of each one of our galaxies in Table 1 and we fit for both the PA_{kin} and q_{kin} parameters, where we find that these can be reliably constrained (i.e. they do not excessively vary as a function of the galactocentric radius within the different elliptical annuli). If this is not the case, then we fix them to the corresponding photometric values, i.e. $PA_{\text{kin}} = PA_{\text{phot}}$ and $q_{\text{kin}} = q_{\text{phot}}$ (see Table 1), of the galaxies for more stable results during the fit. We find this to be mostly the case for q_{kin} , which is generally hard to constrain even in the presence of well-sampled datasets (Foster et al. 2016), and has been, therefore, usually fixed to the photometric value in many previous works (e.g. Foster et al. 2011, 2013, 2016; Bellstedt et al. 2017; Dolfi et al. 2020). Overall, we find that whether we fix or fit for q_{kin} , the shape of the derived rotation

¹ <http://davor.krajnovic.org/id1/>

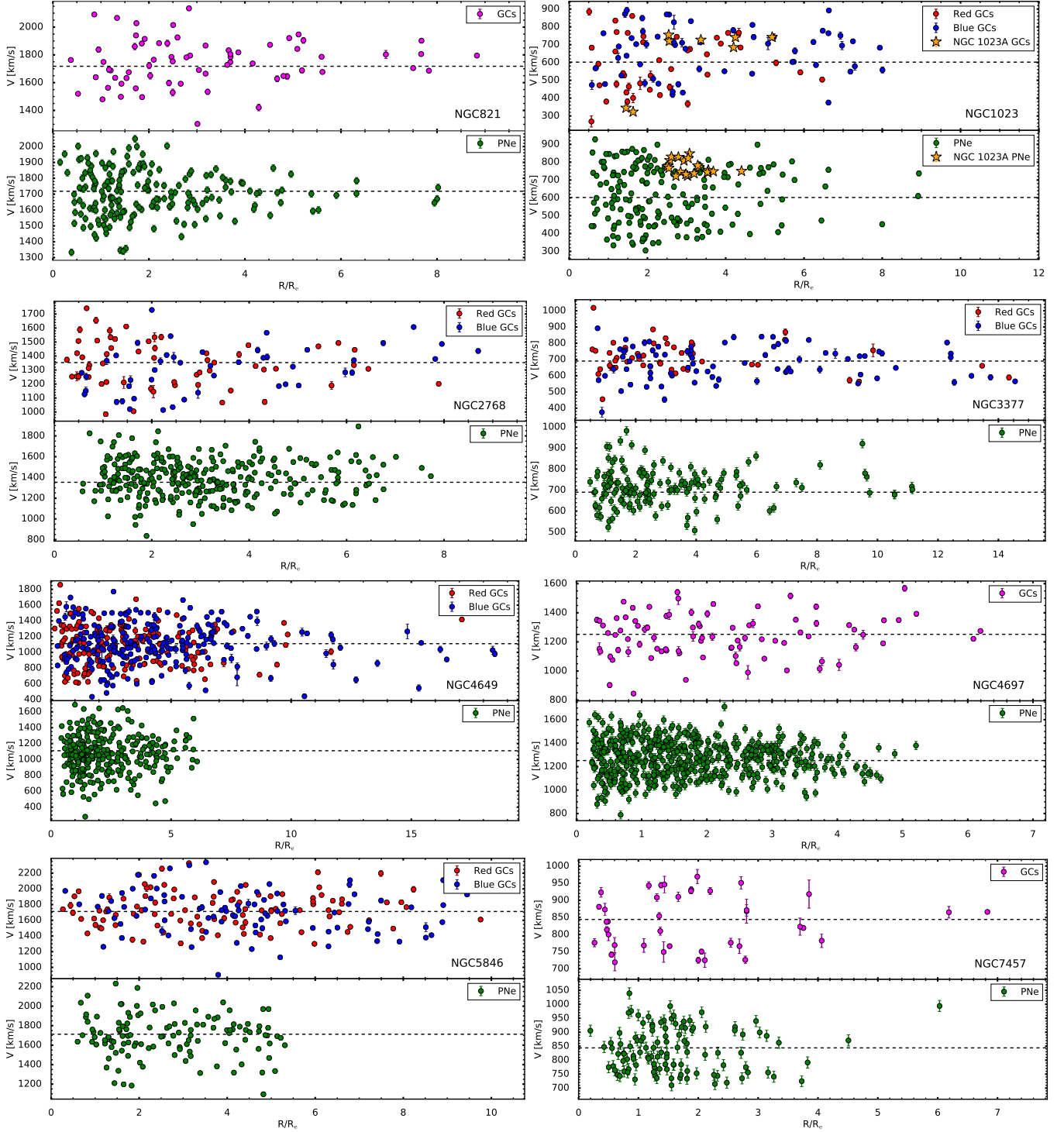


Figure 1. Phase space diagrams showing the measured radial velocities of the GC and PNe tracers of each galaxy as a function of the galactocentric radius, R , divided by the corresponding effective radius of the galaxy, R_e (see Table 1). The red, metal-rich and blue, metal-poor GC sub-populations are represented as red and blue dots, respectively, for all those galaxies for which we identify a colour bimodality distribution, otherwise the GCs are shown as magenta dots. The PNe are shown as green dots. For NGC 1023, we show the 8 GCs and 20 PNe (orange stars) associated to the companion galaxy, NGC 1023A, that we remove from the final catalogues as described in Sec. A1.1.

Table 1. Early-type galaxies selected for study in this work. The main properties of each galaxy, such as morphology, environment, distance, effective radius (R_e), photometric position angle (PA_{phot} measured from North towards East), photometric axial-ratio ($q_{\text{phot}} = 1 - \epsilon_{\text{phot}}$), systemic velocity (V_{sys}) and stellar velocity dispersion within 1 kpc ($\sigma_{1\text{kpc}}$), are taken from (Brodie et al. 2014). The stellar masses are taken from Forbes et al. (2017b) and were calculated from the total $3.6\mu\text{m}$ magnitudes assuming a kroupa initial mass function (Kroupa 2002). Additionally, we quote the total number of spectroscopically confirmed and unique GCs and PNe from the SLUGGS (Forbes et al. 2017a) and eP.N.S (Pulsoni et al. 2018) surveys, respectively, for each galaxy. For the GCs, we specify the adopted colour-split to separate between the red, metal-rich and blue, metal-poor GC sub-populations for all the galaxies where a clear colour bi-modality is observed. For the PNe, we specify the mean error (ΔV) associated with the PNe radial velocity measurements as given in Pulsoni et al. (2018). The values for NGC3115 are those published in Dolfi et al. (2020).

Galaxy name	Morph.	Environm.	Dist. (Mpc)	$\log M^*$ (M_\odot)	R_e (arcsec)	PA_{phot} (degree)	q_{phot}	V_{sys} (kms^{-1})	$\sigma_{1\text{kpc}}$ (kms^{-1})	$N_{\text{GC,tot}}$	GC split (mag)	$N_{\text{GC,red}}$	$N_{\text{GC,blue}}$	N_{PNe}	ΔV (kms^{-1})
NGC 821	E6/S0	Field	23.4	11.00	40	31.2	0.65	1718	193	68	no	-	-	186	21
NGC 1023	SB0	Group	11.1	10.99	48	83.3	0.37	602	183	102	$(g-z) = 1.13$	41	61	183	14
NGC 2768	E6/S0	Group	21.8	11.21	63	91.6	0.43	1353	206	104	$(Rc-z) = 0.57$	58	46	315	20
NGC 3115	S0	Field	9.4	10.93	35	40	0.34	663	248	191	$(g-i) = 0.93$	100	91	189	20
NGC 3377	E5-6	Group	10.9	10.50	36	46.3	0.67	690	135	126	$(g-i) = 0.925$	46	80	152	20
NGC 4649	E2/S0	Cluster	16.5	11.60	66	91.3	0.84	1110	308	430	$(g-z) = 1.2$	179	251	298	20
NGC 4697	E6	Group	12.5	11.15	62	67.2	0.68	1252	180	86	no	-	-	531	35
NGC 5846	E0-1/S0	Group	24.2	11.46	59	53.3	0.92	1712	231	192	$(g-i) = 0.95$	102	90	124	21
NGC 7457	S0	Field	12.9	10.13	36	124.8	0.53	844	74	40	no	-	-	113	20

velocity and velocity dispersion profiles as a function of the galactocentric radius does not significantly change.

The 1D kinematic profiles of the distinct tracers (i.e. GCs, PNe and stars) of each galaxy in Table 1 are shown in Fig. 3. Each sub-figure of Fig. 3 represents one individual galaxy, with the derived PA_{kin} and q_{kin} (where fitted), rotation velocity, V_{rot} , velocity dispersion, σ , and rotation velocity to velocity dispersion, V_{rot}/σ , profiles shown from the top to the bottom panel, respectively. The PA_{kin} is always measured from North towards East for consistency with the 2D kinematic maps in Fig. 2 and A1-A8 and with the PA_{phot} of the galaxy shown in Table 1. The 1-sigma errors of the PA_{kin} and q_{kin} profiles are calculated from running **kinemetry** on 500 bootstrapped samples obtained from sampling with replacement the original kinematic datasets. On the other hand, the 1-sigma errors of the rotation velocity and velocity dispersion profiles are the standard errors of the mean, calculated from the standard deviation of the velocity and velocity dispersion measurements of the data points in each elliptical annuli², divided by the square root of the number of objects in each bin. We also include the 1D kinematic profiles of NGC 3115, where the 1-sigma errors of the V_{rot} and σ profiles are also the standard errors of the mean for consistency with the other galaxies, for the comparison. However, we refer the reader to Dolfi et al. (2020) for the detailed description of the main kinematic features of NGC 3115.

3.2 The kinematic behaviour of the galaxies

From the 2D kinematic maps in Fig. 2 and A1-A8, and from the 1D kinematic profiles in Fig. 3, we find that six galaxies (i.e. NGC 1023, NGC 2768, NGC 3115, NGC 3377, NGC 4697 and NGC 7457) show good kinematic alignment of the GC sub-populations and PNe with respect to the underlying stars (hereafter, *aligned* galaxies). Specifically, four of the galaxies (i.e. NGC 1023, NGC 2768, NGC 3115, NGC 4697 and NGC 7457) have the PA_{kin} of both the GCs and PNe that are closely

aligned with the PA_{kin} of the underlying stars (that is, in turn, closely aligned with the PA_{phot} of the galaxy given in Table 1), as they are consistent within the 1-sigma errors. Additionally, the PA_{kin} of both the GCs and PNe in these four galaxies do not show significant scatter around the PA_{kin} of the underlying stars, but they all display rotation along the photometric major-axis of the galaxy, as it can be seen also from the 2D kinematic maps in Fig. 2, A1, A3, A4 (and in fig. 6 of Dolfi et al. (2020) for NGC 3115).

An exception is NGC 3377, whose blue GC sub-population does not show evidence of a significant rotation (see Fig. A2 and Fig. 3). Additionally, the PNe of NGC 3377 show a possible twist in the PA_{kin} between $\sim 3-5R_e$ and evidence of such a kinematic twist of the PNe was also previously seen by Coccato et al. (2009). However, the PNe show rotation that is closely aligned to that of the underlying stars, as well as red GCs, within the inner $\sim 3R_e$. At larger radii, we see that the rotation of the PNe is still overall consistent with the photometric major-axis of the galaxy from the 2D kinematic maps. Therefore, we also include NGC 3377 in the group of the *aligned* galaxies.

On the other hand, the remaining three galaxies show kinematic misalignments of the GC sub-populations and PNe with respect to the underlying stars, i.e. NGC 821 and NGC 4649, or no net rotation, i.e. NGC 5846 (hereafter, *mis-aligned* galaxies). Specifically, NGC 4649 shows the largest scatter in the PA_{kin} of the PNe and blue GC sub-population with respect to the underlying stars, with clear kinematic twists and minor-axis rotation beyond $\sim 2R_e$. On the other hand, the red GCs of NGC 4649 have PA_{kin} that is slightly offset from that of the stars, but it does not show significant variations as a function of the radius (Fig. 3 and A7). Similarly, in NGC 821, the PNe are rotating more closely aligned to the photometric minor-axis of the galaxy and the GCs are also rotating along a PA_{kin} that is offset from the photometric major-axis of the galaxy (Fig. A5) and consistent with the large 1-sigma errors in the 1D kinematic profiles in Fig. 3.

Finally, in NGC 5846, we are not able to reliably recover the PA_{kin} of the stars, PNe and GC sub-populations. However, from the 2D kinematic maps in Fig. A8, we do not see evidence of any ordered rotation around the galaxy and therefore, of any possible kinematic alignment between the distinct

² These are the same concentric elliptical annuli used in the **kinemetry** algorithm to recover the 1D kinematic profiles at the different galactocentric radii.

tracers. For this reason, we include these three galaxies (i.e. NGC 821, NGC 4649 and NGC 5846) in the group of the *mis-aligned* galaxies.

The different kinematic behaviours of the *aligned* and *mis-aligned* galaxies would suggest different formation histories for these two galaxy groups, with the latter being, possibly, the result of more recent interaction and merger events that have perturbed the dynamical equilibrium state of the galaxies. In Table 2, we summarize the kinematic alignment or misalignment of the GC and PNe tracers with respect to the underlying stars (from SLUGGS) and we indicate whether the red and blue GC sub-populations are kinematically aligned for each galaxy, based on the 2D and 1D kinematic results shown in the Fig. A1-A8 and in Fig. 3, respectively, and described in more detail in the Appendix A for each individual galaxy.

In Fig. 3, we compare together the 1D kinematic profiles of the stars, PNe and GC sub-populations of the *aligned* (top) and *mis-aligned* (bottom) galaxies, with the aim of identifying common trends in their behaviours. Therefore, in Fig. 3, we show the V_{rot} , σ and V_{rot}/σ profiles (from left to right) for the stars (from SLUGGS), PNe, red GCs, blue GCs and all GCs (if no colour bimodality distribution is observed) from the top to the bottom panel, respectively. We also include NGC 3115 for the comparison with the *aligned* galaxies, with its kinematic profiles taken from Dolfi et al. (2020). We notice that the V_{rot}/σ profiles of the *aligned* and *mis-aligned* galaxies have very similar shapes to the corresponding V_{rot} profiles. Therefore, we focus in this section on describing the common features of the V_{rot}/σ profiles of the different kinematic tracers of the galaxies.

We notice that the velocity dispersion profiles of the *aligned* and *mis-aligned* galaxies in Fig. 3 all show weakly decreasing or overall flat behaviours out to large radii, with the exception of NGC 1023, whose PNe and GC sub-populations are characterized by slightly rising velocity dispersion profiles beyond $\sim 2R_e$.

For the *aligned* galaxies in Fig. 3, we notice that their V_{rot}/σ profiles show clearly peaked (NGC 1023, NGC 3115) to flatter (NGC 2768, NGC 3377, NGC 4697) behaviours. NGC 7457 also show a peaked V_{rot}/σ profile, as seen from the GCs at $\sim 2R_e$, even though both the stars and PNe show rising V_{rot}/σ out to $\sim 2\text{--}2.5R_e$. It is worth noticing here that all *aligned* galaxies have blue GCs that are rotating, with the exception of NGC 3377 that shows very low rotation in its blue GC sub-population, with $V_{\text{rot}}/\sigma \lesssim 0.5$ out to large radii. Additionally, while NGC 1023 and NGC 2768 have overall consistent V_{rot}/σ profiles between the red and blue GC sub-populations, the blue GCs of NGC 3115 are characterized by a peak of the $V_{\text{rot}}/\sigma \sim 1.5$ located at larger radii (i.e. $\sim 3R_e$) than that of the red GCs (i.e. $\sim 1\text{--}1.5R_e$).

The *mis-aligned* galaxies in Fig. 3 are, instead, characterized by more peculiar V_{rot}/σ profiles. Only NGC 821 shows an overall flatter V_{rot}/σ profile out to large radii, similarly to NGC 2768, NGC 3377 and NGC 4697. However, in NGC 821, the rotation of the PNe and GCs occurs more closely aligned to the photometric minor-axis of the galaxy. On the other hand, NGC 5846 shows spheroid-like kinematics (i.e. $V_{\text{rot}}/\sigma < 0.5$) out to large radii, while NGC 4649 shows the more interesting double-peaked V_{rot}/σ profiles, as seen from the PNe and red GCs (see Appendix A) for a more detailed

description of the kinematic profiles of these two individual galaxies).

Finally, we look for any mass or environment dependence in the 1D kinematic profiles of our galaxies. Some previous works have found differences in the stellar kinematics of S0 galaxies in different environments, with S0s located in clusters and large groups being more rotationally supported than S0s found in isolation or in small groups (e.g. Deeley et al. 2020; Coccato et al. 2020). This might suggest different formation pathways for cluster and field S0s. However, we do not find any clear dependence on the environment in our kinematic profiles, nor more specifically in the V_{rot}/σ profiles. We argue that this is likely due to the small galaxy sample size that we are using and to the fact that our sample only contains one cluster (i.e. NGC 4649) and three field (i.e. NGC 821, NGC 3115 and NGC 7457) S0s, while the remaining galaxies are located in groups. Therefore, we are missing the high density environments of galaxy clusters.

On the other hand, we do find a dependence of the velocity dispersion profiles on the stellar mass of the galaxies for all our kinematic tracers (i.e. stars, PNe and GCs), with the more massive galaxies showing higher velocity dispersion profiles than the less massive ones, as expected and also observed in previous works (e.g. Foster et al. 2018). At the same time, we also find a stellar mass dependence of the V_{rot}/σ profiles of the stars, PNe and GC sub-populations, with low mass galaxies showing higher V_{rot}/σ profiles than more massive ones. This is, again, consistent with the general picture from previous observational results, in which fast rotators are typically found among the population of low mass galaxies, while slow rotators are found among the class of rounder and more massive galaxies (e.g. Cappellari et al. 2013).

4 DISCUSSION

4.1 Do the PNe and GC sub-populations follow the rotation of the stars?

In Fig. 3, we see that the PNe are overall good tracers of the kinematics of the stars in the overlapping radii out to $\sim 2\text{--}3R_e$ for the *aligned* galaxies, suggesting that we can use the PNe as proxies of the dynamics of the stars out to larger radii (e.g. Coccato et al. 2009, 2013; Cortesi et al. 2016; Zanatta et al. 2018). We see that the red GCs also show a good agreement with the kinematics of the stars out to similar radii. The blue GCs show overall consistent rotation with that of red GCs within the 1-sigma errors in NGC 1023 and NGC 2768, suggesting that both GC sub-populations are likely tracing the kinematic properties of the same underlying stellar population in these two *aligned* galaxies. The blue GCs are also rotating in NGC 3115, however their rotation velocity peaks at larger radii (i.e. $\sim 3R_e$) than that of the red GCs (i.e. $\sim 1\text{--}2R_e$), possibly suggesting differences in the formation history of NGC 3115 as compared to NGC 1023 and NGC 2768, e.g. different properties of the merger event, that we discuss in more details in Sec. 4.2. On the other hand, the blue GCs in NGC 3377 show very little amount of rotation at all radii as compared to the red GCs, suggesting that they are likely tracing the kinematic properties of the underlying stellar population of the galaxy halo, with some blue GCs that may also have an ex-situ origin (e.g. Forbes et al. 1997; Forbes & Rebus 2018).

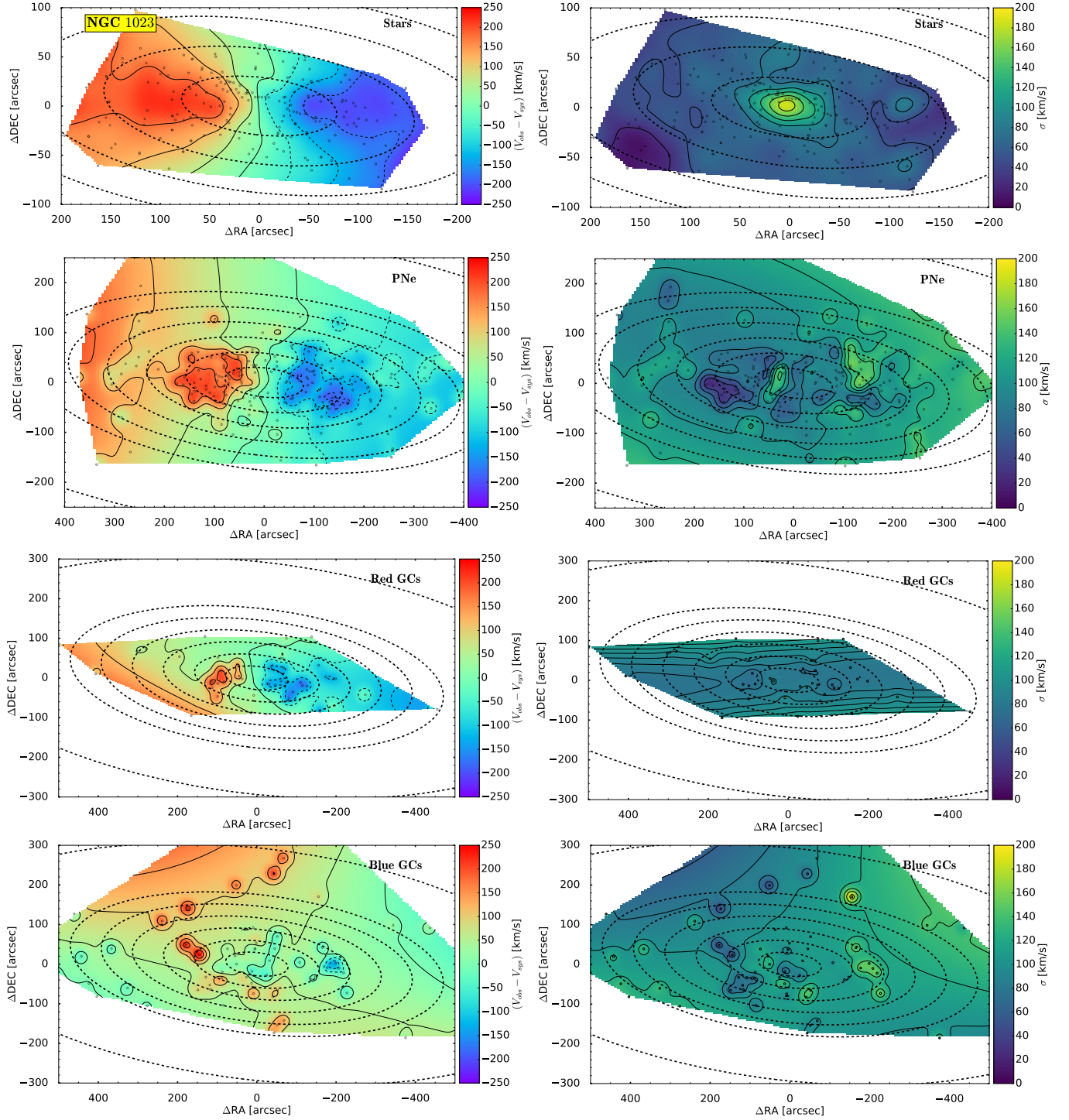


Figure 2. From top to bottom, 2D velocity (left-hand side) and velocity dispersion (right-hand side) maps of the SLUGGS stars, PNe, red and blue GCs for NGC 1023, shown here as an example (the 2D kinematic maps of the remaining eight galaxies in Table 1 are shown in the Figures A1-A8). North is up, East is left. The small open circles indicate the positions of the tracers, the black solid lines indicate the iso-velocity contours and the black dashed lines represent the $1\text{-}6R_c$ and $10R_c$ photometric ellipses, which are inclined by the PA_{phot} of the galaxy. The PA_{phot} is measured from North towards East. The 2D maps are normalized with respect to the velocity scale bar on the right of each map.

Aligned galaxies

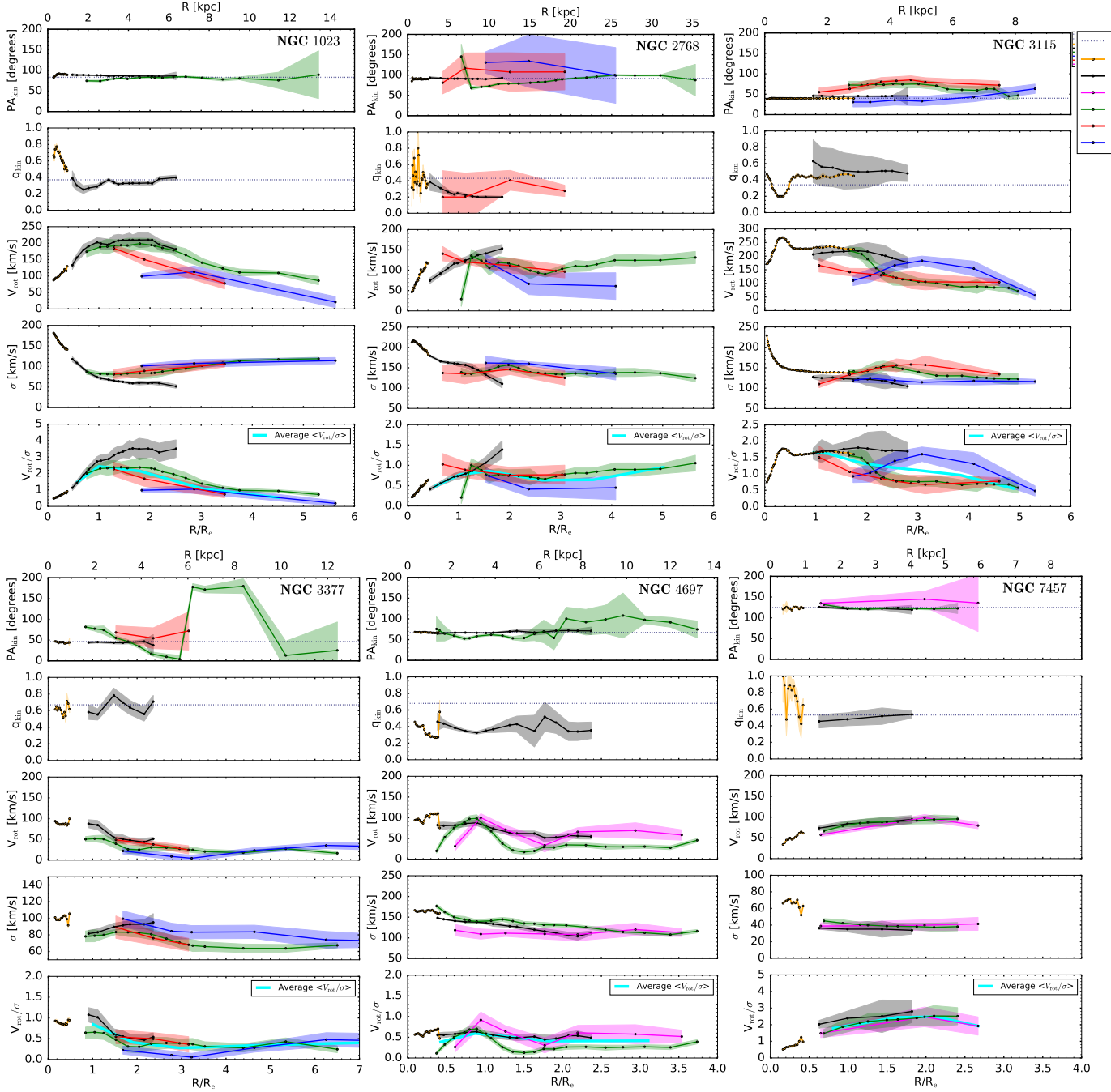


Figure 3. 1D kinematic profiles for the ATLAS^{3D}, or MUSE for NGC 3115 (orange line), and SLUGGS (black line) stars, PNe (green line), red and blue GCs (red and blue lines, respectively) and all GCs (magenta line) for those galaxies with no bimodal color distribution in the GC population (see Table 1). Each column represents one individual galaxy, which are being grouped based on whether they are *aligned* or *mis-aligned*. NGC 3115 is taken from Dolfi et al. (2020). From top to bottom in each panel, we show the derived 1D profiles of the kinematic position angle, PA_{kin} , kinematic axial-ratio, q_{kin} , rotation velocity, V_{rot} , velocity dispersion, σ , and rotation velocity to velocity dispersion, V_{rot}/σ . For the *aligned* galaxies, we also show the smooth V_{rot}/σ profile (cyan line), calculated by averaging the individual V_{rot}/σ profiles of the distinct kinematic tracers in the overlapping radii for each galaxy. For NGC 4697, we only fit for the PA_{kin} and we keep q_{kin} fixed to the photometric value, q_{phot} , of the galaxy (see Table 1) for all our kinematic datasets, while, for NGC 5846, we keep both PA_{kin} and q_{kin} fixed to the photometric values, PA_{phot} and q_{phot} , of the galaxy.

Mis-aligned galaxies

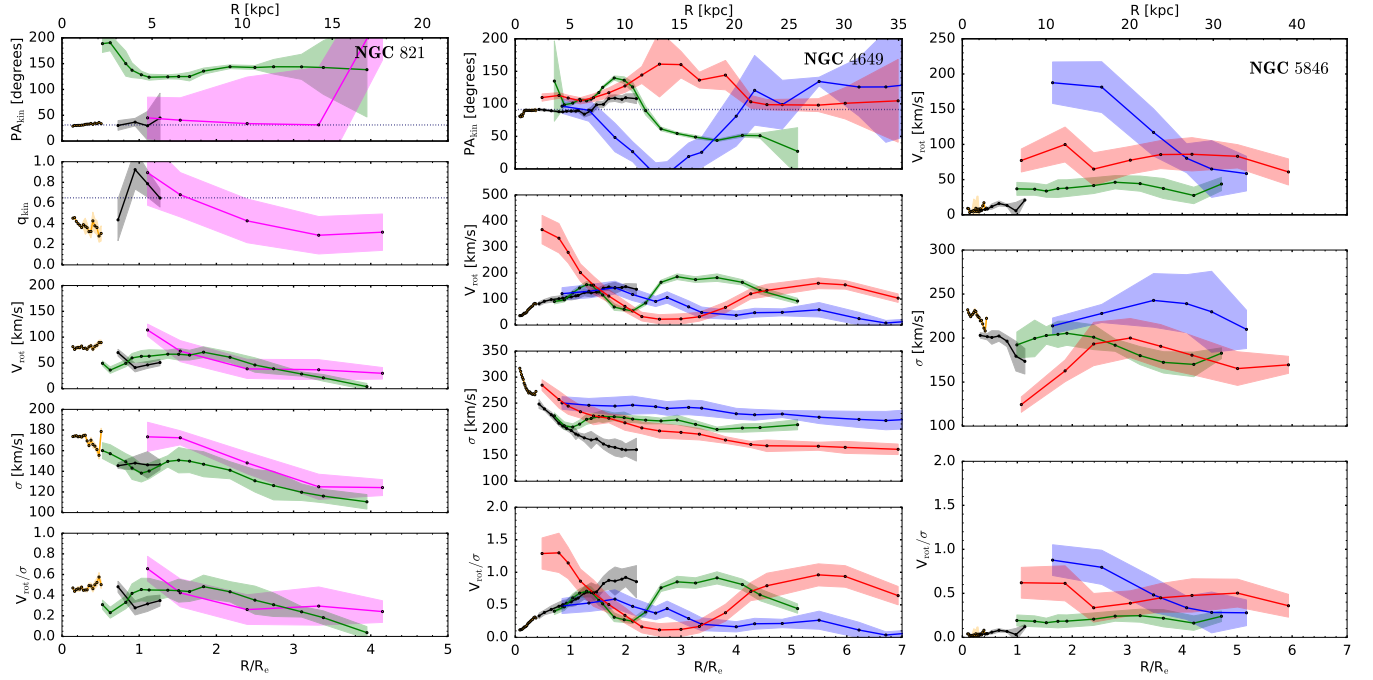
Figure 2. *Continued.*

Table 2. Summary table indicating whether the GC sub-populations and PNe are kinematically aligned to the underlying stars and whether the red and blue GC sub-populations are also kinematically aligned in each galaxy, i.e. their PA_{kin} are consistent within the 1-sigma errors based on the 2D kinematic maps and 1D kinematic profiles. If no colour bimodality distribution is observed, then all (red+blue) GCs are used. We assign "X" if there is no alignment between the pair of tracers that we are comparing in each galaxy and "✓" if there is alignment. The results for NGC 3115 are taken from [Dolfi et al. \(2020\)](#).

Galaxy	Stars vs. PNe	Stars vs. Red GCs	Stars vs. Blue GCs	Stars vs. GCs	Red GCs vs. Blue GCs
NGC 821	X	-	-	X	-
NGC 1023	✓	✓	✓	-	✓
NGC 2768	✓	✓	✓	-	✓
NGC 3115	✓	✓	✓	-	X
NGC 3377	✓	✓	X	-	X
NGC 4649	X	✓	X	-	X
NGC 4697	✓	-	-	✓	-
NGC 5846	X	X	X	-	X
NGC 7457	✓	-	-	✓	-

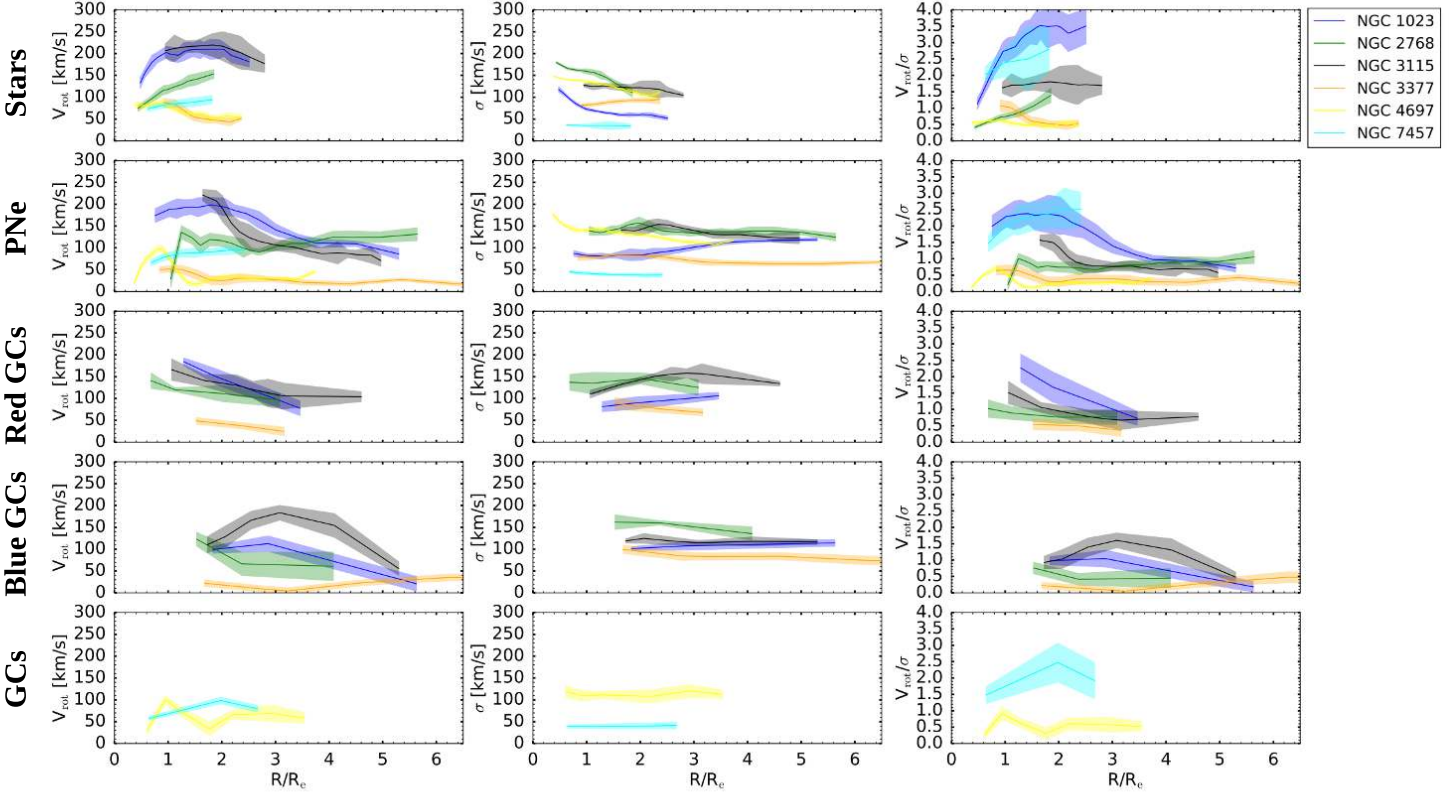
The *mis-aligned* galaxies show more interesting kinematic behaviours, as both the PNe and GC sub-populations display minor-axis rotation and kinematic twists with respect to the underlying stars (i.e. NGC 821 and NGC 4649). NGC 5846 is also an example of a non-rotating galaxy. These kinematic behaviours suggest a more complex formation histories for the *mis-aligned* galaxies, with, possibly, recent merger and accretion events.

4.2 How did the *aligned* galaxies form?

We have seen that the six *aligned* galaxies show good kinematic alignment of both the PNe and GC tracers with respect to the underlying stars in the overlapping radii. In Fig. 4, we now calculate their V_{rot}/σ profiles by averaging

the contributions of the individual V_{rot}/σ profiles of the distinct kinematic tracers (i.e. stars, PNe and GCs) of each galaxy in the overlapping radii. The shaded areas represent the 1-sigma standard errors of the mean. The inset plot shows the gradients, as adopted in the *Magneticum* simulations by [Schulze et al. \(2020\)](#), to classify their simulated ETGs as *flat* (i.e. $-0.04 < V_{rot}/\sigma < 0.04$), *increasing* (i.e. $V_{rot}/\sigma > 0.04$) and "peaked and decreasing" (hereafter, *peaked*; i.e. $V_{rot}/\sigma < -0.04$) from the stellar kinematics extending out to $\sim 5R_e$. From the comparison of the observed V_{rot}/σ profiles of the six *aligned* galaxies in Fig. 4 with the gradients from [Schulze et al. \(2020\)](#), we classify NGC 1023, NGC 3115, NGC 3377 and NGC 7457 as *peaked*, while NGC 2768 and NGC 4697 as *flat*.

Aligned galaxies



Mis-aligned galaxies

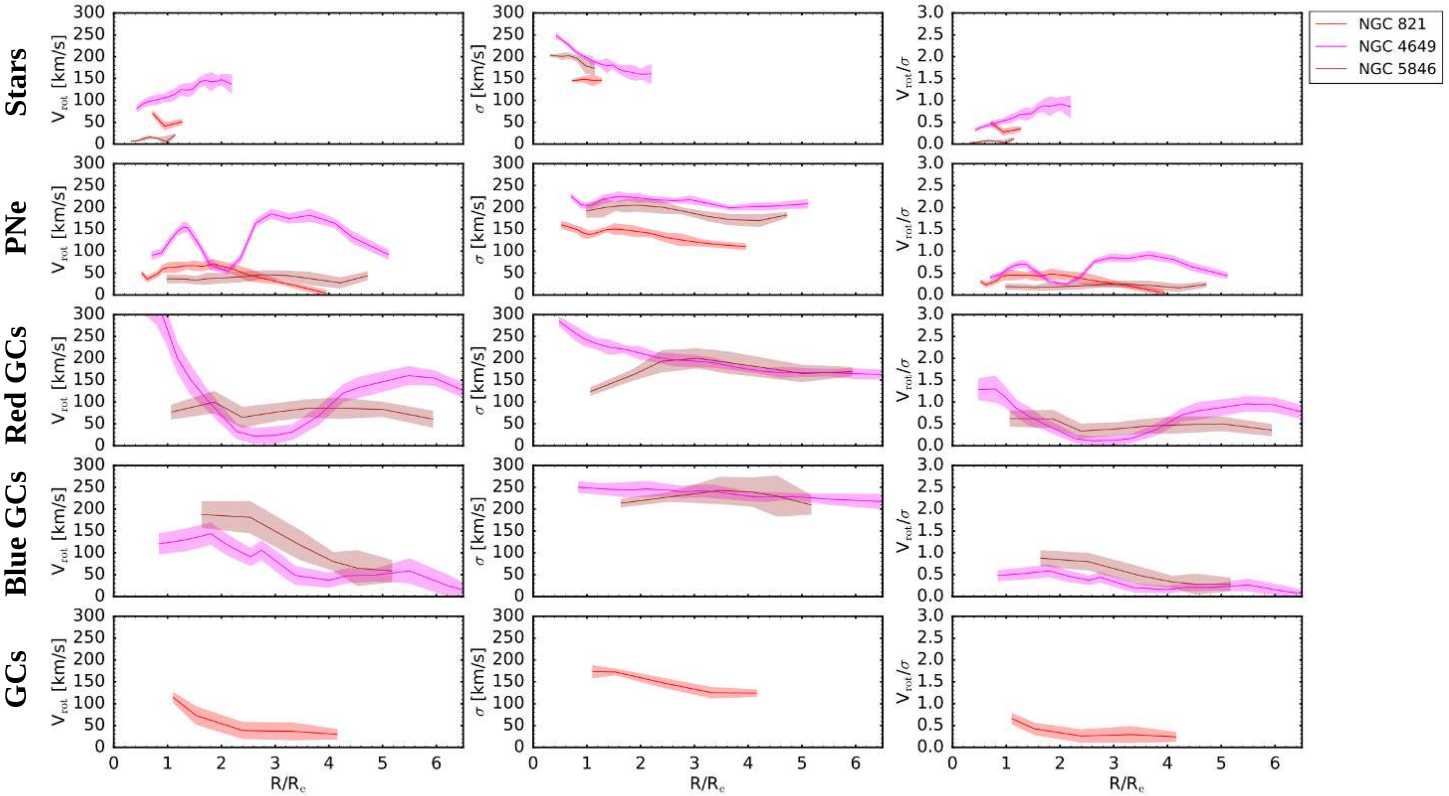


Figure 3. 1D kinematic profiles of the *aligned* (top) and *mis-aligned* (bottom) galaxies compared together. The V_{rot} , σ and V_{rot}/σ profiles are shown from left to right, respectively, while the kinematic profiles of the stars (from SLUGGS), PNe, red GCs, blue GCs and all GCs (if no colour bimodality distribution is observed) are shown from the top to the bottom panel, respectively. The kinematic profiles are the same as in Fig. 3, with the addition of NGC 3115 (Dolfi et al. 2020) among the *aligned* galaxies.

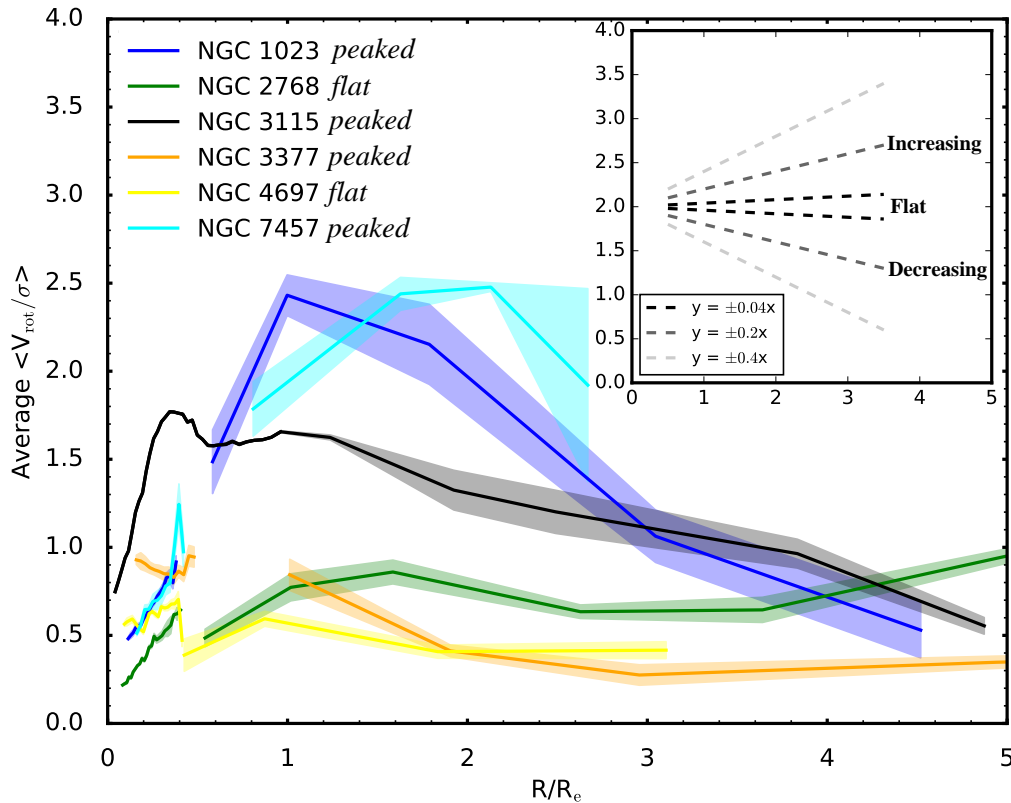


Figure 4. Smooth V_{rot}/σ profiles for the six *aligned* galaxies, calculated by averaging the individual V_{rot}/σ profiles of the distinct kinematic tracers (i.e. stars, PNe and GCs) of each galaxy in the overlapping radii. The shaded areas represent the corresponding 1-sigma standard errors of the mean at the radii where the average V_{rot}/σ profile is calculated. The inset plot shows six linear functions characterized by different slopes, i.e. ± 0.04 , ± 0.2 , ± 0.4 . The ± 0.04 slope corresponds to the V_{rot}/σ gradient adopted by [Schulze et al. \(2020\)](#) to separate the *flat* V_{rot}/σ profiles from the *increasing* ($V_{\text{rot}}/\sigma > 0.04$) and *peaked* ($V_{\text{rot}}/\sigma < -0.04$) V_{rot}/σ profiles. The ATLAS^{3D} data are also shown in this plot, however they typically do not reach beyond $\sim 0.5R_e$ and, therefore, do not overlap in radius with the other kinematic tracers (with the exception of the MUSE data of NGC 3115).

4.2.1 Galaxies with peaked V_{rot}/σ profiles

The four galaxies (i.e. NGC 1023, NGC 3115, NGC 3377, NGC 7457) with *peaked* V_{rot}/σ profiles should share similar accretion histories in more recent times (i.e. $z \lesssim 1$) according to [Schulze et al. \(2020\)](#), dominated by minor ($1:10 < \text{mass-ratio} < 1:4$) and mini ($\text{mass-ratio} < 1:10$) mergers that enhanced the velocity dispersion of the galaxy outer regions without disrupting its central disk-like kinematics. Some of these *peaked* galaxies may have also experienced a major merger ($\text{mass-ratio} > 1:4$), however this is most likely to have occurred at early times, i.e. more than 5 Gyr ago. In any case, [Schulze et al. \(2020\)](#) find that more than half of the population of the *peaked* galaxies (i.e. $\sim 60\%$) is likely to have experienced no major mergers in its past evolutionary history.

Using the Illustris TNG100 simulations, [Pulsoni et al. \(2020\)](#) studied the accretion histories of a sample of ETGs in the stellar mass range $10^{10.3} \leq M^*/M_\odot \leq 10^{12}$, reaching out to $15R_e$. They find overall consistent results with those from [Schulze et al. \(2020\)](#), where galaxies with *peaked* V_{rot}/σ profiles have typically lower stellar masses and have evolved mostly passively after having, possibly, experienced a gas-rich major merger at early times (i.e. $z > 1$). Although a significant fraction (i.e. $\sim 60\%$) of the galaxies with *peaked* V_{rot}/σ profiles may have not experienced any major merger and have only

evolved through the accretion of low-mass galaxies in minor and mini mergers that influenced the outer galaxy regions, the gas-rich nature of these merger events may still play an important role. Indeed, [Pulsoni et al. \(2020\)](#) find that the peak of rotation in galaxies with *peaked* V_{rot}/σ profiles becomes less prominent as the fraction of ex-situ stars accreted through major mergers increases. However, the peak in rotation can re-establish itself if new ($z \leq 1$) stars are formed within the galaxy from its cold gas, either in-situ or recently accreted through mergers. This is true for both fast and slow rotator galaxies (see their figure 8).

Finally, even though mini mergers do not largely affect the central peak of rotation of the galaxies with *peaked* V_{rot}/σ profiles, they can increase the stellar rotation of the galaxies at larger radii if high fractions of the stellar mass (i.e. 10–30%) are accreted through this channel ([Pulsoni et al. 2020](#)). This mild increase of the stellar V_{rot}/σ at larger radii could be a consequence of the orbital configuration of the merger, as [Karademir et al. \(2019\)](#) have shown with simulations that mini mergers can increase the size of the host galaxy disk if they occur along the disk plane. Therefore, these mini mergers could produce galaxies with extended stellar disks characterized by, possibly, higher rotation out to larger radii.

NGC 1023 and NGC 3115 are more massive than NGC 3377 and NGC 7457. For this reason, NGC 1023 and NGC

3115 should be more similar to the Class II galaxies of [Pulsoni et al. \(2020\)](#), that are in-situ dominated in the inner regions and ex-situ dominated in the outskirts of the galaxies. On the other hand, NGC 3377 and NGC 7457 should have more similar properties to the Class I galaxies of [Pulsoni et al. \(2020\)](#), that are in-situ dominated at all radii. Therefore, this suggests that NGC 3377 and NGC 7457 have, on average, accreted larger (i.e. up to $\sim 50\text{-}60\%$) gas fractions than NGC 1023 and NGC 3115 (i.e. up to $\sim 30\text{-}40\%$), possibly through an early gas-rich major merger, that contributed to the in-situ star formation of the galaxies. This merger event is expected to have occurred at earlier times, i.e. $z \geq 2$, for NGC 3377 and NGC 7457 as compared to NGC 1023 and NGC 3115, i.e. $1 < z < 2$, while no major mergers have likely happened in the evolution histories of all four galaxies since $z = 1$ ([Pulsoni et al. 2020](#); [Schulze et al. 2020](#)).

However, NGC 1023, NGC 3115 and NGC 7457 are rotationally supported S0 galaxies, with $V_{\text{rot}}/\sigma > 1$ out to $\sim 3R_e$, as seen in Fig. 4. Following [Bournaud et al. \(2005\)](#), a mean $V_{\text{rot}}/\sigma > 1$ is more compatible with a minor merger rather than a major one, which would produce hotter disk kinematics with mean $V_{\text{rot}}/\sigma < 1$. For this reason, NGC 1023 and NGC 7457 are more consistent with having experienced at most a minor merger with mass-ratio 1:10, due to their high $V_{\text{rot}}/\sigma > 2$ ([Bournaud et al. 2005](#)). On the other hand, NGC 3115 is more consistent with a minor merger with mass-ratio 1:7 that resulted in its $1 < V_{\text{rot}}/\sigma < 2$ ([Bournaud et al. 2005](#)) as seen in Fig. 4. Indeed, for NGC 3115, [Dolfi et al. \(2020\)](#) have proposed a scenario in which the galaxy was originally a spiral that experienced an early (i.e. $\sim 9\text{Gyr}$ ago) gas-rich minor merger in the mass-ratio range 1:4-1:10, which shaped its current embedded kinematically cold disk. In more recent times, NGC 3115 has evolved mostly passively, exhausting its own gas through in-situ star formation and accreting low-mass dwarf galaxies in mini mergers that produced the spheroid-like kinematics of the outer regions of the galaxy. This formation scenario for NGC 3115 is consistent with the stellar population results from [Poci et al. \(2019\)](#), who found a dominant old (i.e. $\sim 9\text{Gyr}$), metal-rich stellar population in the kinematically cold disk component of NGC 3115, therefore ruling out the occurrence of recent major or minor merger events that would likely destroy this disk structure. At the same time, the old and metal-poor stellar population with hotter kinematics found in the stellar halo of NGC 3115 suggests a late accretion of low-mass dwarf galaxies in dry minor and mini mergers onto the outer regions of the galaxy.

For NGC 1023, we propose a similar formation history as for NGC 3115, characterized by an early (i.e. $1 < z < 2$) gas-rich minor merger with mass-ratio 1:10. This gas-rich minor merger would be consistent with the high stellar $V_{\text{rot}}/\sigma > 2$ of NGC 1023 (see Fig. 3), according to [Bournaud et al. \(2005\)](#), and would shape the embedded kinematically cold disk of NGC 1023, according to [Naab et al. \(2014\)](#). Moreover, NGC 1023 is classified as an SB0 galaxy from previous photometric studies that detected the presence of a barred bulge ([Barbon & Capaccioli 1975](#)). From simulations, [Cavanagh & Bekki \(2020\)](#) have shown that bars can be formed from both major and minor mergers and that the orbital configuration of the merger plays a decisive role in determining whether the bar can survive after the merger. Specifically, they found that minor mergers with mass-ratio 1:10 and closely aligned spin angles are most conducive to the bar formation. Therefore,

this seems to reinforce our proposed scenario that NGC 1023 formed through an early gas-rich minor merger with mass-ratio 1:10, where the merging galaxies had similar orientations of their spin angles. The V_{rot}/σ profiles of the red and blue GCs that show little rotation at larger radii (see Fig. 3) would also be more consistent with a minor merger scenario, according to [Bekki et al. \(2005\)](#). [Cortesi et al. \(2016\)](#) have also found that the majority of the red GCs (and a small fraction of the blue GCs) are associated with the disk of NGC 1023 and, therefore, show a similar disk-like kinematics as the stars and PNe. These GCs could have, thus, formed together with the disk of NGC 1023 at early times (i.e. $z \sim 2$) and, possibly, at the epoch of the early gas-rich minor merger. At late times, NGC 1023 has likely continued its evolution history through the accretion of dwarf galaxies in mini mergers ([Schulze et al. 2020](#)). Indeed, NGC 1023 is currently ongoing an interaction with its companion dwarf galaxy, NGC 1023A, suggesting that NGC 1023 is still experiencing its late mini merger accretion. The HI gas cloud detected around NGC 1023, with its asymmetric spatial distribution ([Sancisi et al. 1984](#); [Capaccioli et al. 1986](#)), could be the result of the gas that was stripped from the dwarf galaxies accreted by NGC 1023 in mini mergers, as previously suggested also by [Cortesi et al. \(2016\)](#). Finally, [Corsini et al. \(2016\)](#) detected the presence of a nuclear disk in NGC 1023, which is characterized by a younger ($\sim 3.4\text{Gyr}$) and more metal-rich ($[\text{Fe}/\text{H}] = 0.50\text{dex}$) stellar population than the host galaxy bulge, suggesting that it may have formed from pre-processed, metal-enriched gas within NGC 1023. Therefore, the presence of the young nuclear disk would seem to agree with a recent (and, possibly, still ongoing) mini merger accretion in NGC 1023, where the gas stripped from the dwarf galaxies may have been funnelled towards the galaxy central regions, facilitated by the presence of the bar, to form the young and metal-rich nuclear disk of NGC 1023.

Overall, the formation histories of NGC 1023 and NGC 3115 should be very similar, with the main difference being, possibly, in the orbital configuration of the mergers. In Fig. 3, we notice that the blue GCs of NGC 3115 have a V_{rot}/σ peak located at larger radii (i.e. $\sim 3R_e$) than the red GCs (i.e. $\sim 1R_e$). On the other hand, the red and blue GCs of NGC 1023 have similar V_{rot}/σ profiles. According to [Bekki et al. \(2005\)](#), minor mergers can produce a rotation velocity difference between the blue and red GCs, as we see for NGC 3115 in Fig. 3. The fact that we do not see this rotation velocity difference in the red and blue GCs of NGC 1023, that also formed through a minor merger of similar mass-ratio, could suggest different orbital configurations of the minor mergers in NGC 1023 and NGC 3115. Alternatively, [Karademir et al. \(2019\)](#) showed that mini mergers occurring along the disk plane of the galaxy can increase the size of the host galaxy disk. Therefore, this could suggest that the mini mergers in NGC 3115 have occurred along the plane of the disk, causing the size of the disk to increase. As a result, we see a more extended disk-like kinematics in NGC 3115 than in NGC 1023. Additional simulations of GC kinematics would be required in order to understand whether a specific orbital configuration of the minor and mini mergers can, indeed, produce the observed rotation velocity difference in the red and blue GCs of NGC 3115, as compared to NGC 1023.

Similarly to NGC 1023, NGC 7457 should have also formed through a gas-rich minor merger with mass-ratio 1:10, which

would be more consistent with its high stellar $V_{\text{rot}}/\sigma > 2$ (see Fig. 3), according to (Bournaud et al. 2005). However, according to Pulsoni et al. (2020), low-mass galaxies, such as NGC 7457, should be in-situ dominated at all radii, with very large gas fractions (i.e. $\sim 50\text{--}60\%$) that were accreted at early times (i.e. $z > 2$) and that contributed to the in-situ star formation of the galaxy until more recently. These galaxies are also expected to have accreted only very few ex-situ stars onto their outskirts from mini mergers. Therefore, this would suggest that the vast majority of the gas fraction in NGC 7457 already belonged to the galaxy (i.e. in-situ origin). From the stellar kinematics, Bellstedt et al. (2017) showed that the high V_{rot}/σ of NGC 7457 was more consistent with that of a disk progenitor galaxy that evolved passively through secular evolution, consuming its own in-situ gas. Zanatta et al. (2018) also found that $\sim 70\%$ of the GCs of NGC 7457 belong to the disk of the galaxy and closely follow the kinematics of the stars and PNe (as we have also seen in Fig. 3), therefore suggesting mostly an in-situ origin for the GCs and a secular evolution for NGC 7457. According to Schulze et al. (2020), around half (i.e. $\sim 40\%$) of the population of galaxies with *peaked* V_{rot}/σ profiles are found to have experienced no minor mergers. However, they are still likely to have experienced, even multiple (i.e. up to 4), mini mergers in their late (i.e. $z < 1$) evolution histories, which contributed to the few ex-situ stars in the galaxy outskirts. These mini mergers are expected to enhance the dispersion of the galaxy, and of its GCs (Bekki et al. 2005), in the outer regions, without altering the central V_{rot}/σ profiles of NGC 7457's GCs and stars. In Fig. 3, we see that there is a hint that the V_{rot}/σ profile of the GCs starts decreasing beyond $\sim 2R_e$ and such behaviour, even if weak, is also visible from the V_{rot}/σ profile of the GCs in Zanatta et al. (2018). Finally, NGC 7457 shows the youngest ($\sim 6\text{Gyr}$) stellar population (McDermid et al. 2015; Forbes et al. 2017b), with respect to the other galaxies in our sample, suggesting that the galaxy continued to form new stars from its large in-situ gas reservoir during its passive evolution until more recently. Indeed, according to Pulsoni et al. (2020), Class I galaxies, such as NGC 7457, are characterized by the largest fraction ($\sim 50\%$) of in-situ formed stars at $z \leq 1$, with respect to the other classes. Therefore, NGC 7457 seems to be consistent with mostly a secular evolution during which it consumed its own in-situ gas. At late times, NGC 7457 has likely accreted dwarf galaxies in mini mergers that caused the rotation velocity of the GCs to, possibly, decrease beyond $\sim 2R_e$. It would be interesting to extend the stellar and GC kinematics beyond $2R_e$, in order to confirm whether the V_{rot}/σ profiles are, indeed, decreasing, consistent with a spheroid-like kinematics at larger radii produced by the late mini merger accretion.

Similarly to NGC 7457, NGC 3377 should also be mostly in-situ dominated at all radii, with a somewhat larger fractions of ex-situ stars that are accreted through minor and mini mergers (Pulsoni et al. 2020). The stellar $V_{\text{rot}}/\sigma \sim 1$ of NGC 3377 (see Fig. 3) would be consistent with a minor merger with mass-ratio 1:4.5, according to Bournaud et al. (2005). This minor merger was likely gas-rich and occurred early (i.e. $1 < z < 2$), in order to shape the embedded kinematically cold disk of NGC 3377, according to Naab et al. (2014); Schulze et al. (2020). Additionally, the red GCs are following the rotation of the stars (see Fig. 3) in the overlapping radii and they show little rotation at larger radii, which is also

consistent with a minor merger scenario (Bekki et al. 2005). However, it is interesting to note that the red GCs in NGC 3377 are not as old as the red GCs in NGC 3115, as found by (Usher et al. 2019). This would suggest a more recent formation for the red GCs of NGC 3377, as compared to the red GCs of NGC 3115, possibly after the epoch of the gas-rich minor merger that produced the host galaxy disk. A fraction of the GCs in NGC 3377 could also have an ex-situ origin. Indeed, the results from Usher et al. (2019) showed that the GCs of NGC 3377 display a wide range of metallicities, including few very young and metal-poor GCs, suggesting the contribution from recently accreted dwarf galaxies. According to Pulsoni et al. (2020) and Schulze et al. (2020), the late (i.e. $z < 1$) evolution history of NGC 3377 is likely dominated by the accretion of dwarf galaxies in mini mergers, which may have contributed to ex-situ stars as well as to ex-situ GCs in the outer regions of the galaxy. Specifically, the blue GCs in NGC 3377 show very little rotation out to large radii, as compared to the other kinematic tracers in NGC 3377 and to the other galaxies in our sample (see Fig. 3), suggesting that some blue GCs have an ex-situ origin.

4.2.2 Galaxies with flat V_{rot}/σ profiles

The two galaxies with *flat* V_{rot}/σ profiles (i.e. NGC 2768, NGC 4697) should share similar accretion histories according to Schulze et al. (2020) and should be dominated by minor and mini mergers in more recent times (i.e. $z \lesssim 1$), similarly to the *peaked* galaxies. However, galaxies with *flat* V_{rot}/σ profiles are more likely to have experienced also a late (i.e. $z \lesssim 1$) major merger that destroyed the central disk-like kinematics of the galaxy (Schulze et al. 2020). These results are also consistent with those from Pulsoni et al. (2020), who find that the V_{rot}/σ of the galaxies decreases as the ex-situ fraction increases. Therefore, galaxies with *flat* V_{rot}/σ profiles should have typically higher stellar masses, since they have likely experienced more recent ($z \leq 1$) and more gas poor mergers that brought in larger fractions of ex-situ stars, without much gas, flattening the central disk-like kinematics of the galaxy (Pulsoni et al. 2020). NGC 2768 and NGC 4697 are also more massive than the four *peaked* galaxies, therefore they should be characterized by similar in-situ and ex-situ fractions in the inner regions and be ex-situ dominated in the outskirts of the galaxies (i.e. Class III of Pulsoni et al. 2020).

NGC 2768 shows a $V_{\text{rot}}/\sigma \sim 1$ out to large radii from the stars and PNe (see Fig. 3), which would be consistent with a minor merger with mass-ratio 1:4.5, according to Bournaud et al. (2005). However, this merger is likely to have occurred more recently at $z \lesssim 1$ (Schulze et al. 2020; Pulsoni et al. 2020) and to be more gas-poor, as compared to the mergers experienced by the *peaked* galaxies that are typically gas-rich (Pulsoni et al. 2020). Naab et al. (2014) showed that a late ($z < 2$) gas-poor major merger can spin-up the stars in the merger remnant and produce a rising λ_R profile, as seen in figure 5 of Naab et al. (2014), which resembles the rising stellar V_{rot}/σ profile, shown in Fig. 3. However, a gas-poor major merger with mass-ratio $> 1:4$ would produce a galaxy remnant with hotter disk kinematics, i.e. $V_{\text{rot}}/\sigma < 1$ (Bournaud et al. 2005), which would not be entirely consistent with the V_{rot}/σ of NGC 2768. Therefore, we suggest that NGC 2768 likely formed through a late (i.e. $z \lesssim 1$) gas-poor minor merger with mass-ratio $\sim 1:4.5$, as was previously suggested by Zanatta

et al. (2018). This late gas-poor minor merger was likely responsible for producing the kinematic misalignment between the stars and gas in the centre of the galaxy (Sarzi et al. 2006) and the flat V_{rot}/σ profile of the stars and PNe out to larger radii (see Fig. 4). Additionally, the gas-poor minor merger also likely contributed to a fraction of the ex-situ stars, even though a significant fraction of ex-situ stars (i.e. $\sim 20\%$) is expected to come from the mini mergers that also shaped the late ($z < 1$) evolution history of the galaxy (Pulsoni et al. 2020; Schulze et al. 2020). The kinematics of the red and blue GC sub-populations, which show low $V_{\text{rot}}/\sigma \lesssim 1$ out to large radii, is also more consistent with a minor merger scenario (Bekki et al. 2005). Moreover, Forbes et al. (2012) have shown that the red GCs follow the radial density distribution of the bulge PNe and stars and are, therefore, mostly associated with the spheroidal component of the galaxy. This could be consistent with NGC 2768 having undergone a more gas-poor accretion history (Pulsoni et al. 2020) that has produced the spheroid-like kinematics of the GC sub-populations, a fraction of which could likely have an ex-situ origin.

NGC 4697 shows a $V_{\text{rot}}/\sigma \sim 0.5$ (see Fig. 4), which would be consistent with a major merger with mass-ratio 1:3, according to Bournaud et al. (2005). However, the GCs show a V_{rot}/σ that is decreasing at larger radii and this kinematic behaviour is more consistent with a minor merger (Bekki et al. 2005). Bournaud et al. (2005) showed that multiple minor mergers in the mass-ratio range 1:4.5-1:10 can, ultimately, produce an elliptical galaxy with stellar kinematics and morphology that are similar to those of an elliptical galaxy produced through an individual major merger. Therefore, we suggest that NGC 4697 has likely formed through multiple minor mergers (at least two) in the mass-ratio range 1:4.5-1:10. These minor mergers likely occurred more recently (i.e. $z \lesssim 1$) and were gas-poor, as for NGC 2768, therefore contributing to some fraction of the ex-situ stars at all radii (Pulsoni et al. 2020; Schulze et al. 2020). At late times (i.e. $z < 1$), NGC 4697 has likely continued its evolution through the accretion of dwarf galaxies in mini mergers that contributed to the remaining fraction of ex-situ stars (Pulsoni et al. 2020; Schulze et al. 2020). An early work has detected the presence of a young (i.e. ~ 1 Gyr old) stellar population as well as of low levels of ongoing star formation in the central regions of NGC 4697 (Ford & Bregman 2013). According to Pulsoni et al. (2020), galaxies in Class III, such as NGC 4697, may also have accreted some small gas fractions, i.e. $\sim 30\%$, from which new stars can be born. If this gas was funnelled towards the central regions of the galaxy at the time of the minor mergers, then it could have triggered a more recent star formation event that formed the young stars detected by Ford & Bregman (2013) in the galaxy central regions. Alternatively, a more recent star formation event could have been induced from the remaining in-situ gas of NGC 4697 that was funnelled towards the central regions of the galaxy at the epoch of the late gas-poor minor and mini mergers. This young stellar population could, possibly, be associated with the sub-population of bright PNe that was identified by Sambhus et al. (2006), as theoretical studies suggests that such a bright PNe sub-population in ETGs would require high-mass, young (i.e. ≤ 1 Gyr old) stars (Kalirai et al. 2008; Ciardullo 2010). Sambhus et al. (2006) showed that the bright PNe sub-population had an asymmetric distribution and was concentrated near the central regions of the galaxy, but it was not tracing the kinematics of the

underlying stars (Sambhus et al. 2006). Therefore, this could be consistent with a scenario in which this small fraction of young stars in the central regions of the galaxy has formed from the gas, of either in-situ or ex-situ origin, that induced a recent star formation event during the late minor and mini merger accretion of NGC 4697.

4.3 How did the *mis-aligned* galaxies form?

The three *mis-aligned* galaxies show kinematic twists and misalignment of both the PNe and GC sub-populations with respect to the underlying stars. For this reason, they have more peculiar kinematic profiles that cannot be easily linked to one of the three characteristic profile shapes (i.e. *peaked*, *flat*, *increasing*) investigated by Schulze et al. (2020). This suggests, therefore, that these galaxies had a more complex formation history that involved a larger number of recent merger and interaction events.

NGC 821 is an isolated elliptical galaxy that should share a similar accretion history to the Class III galaxies of Pulsoni et al. (2020), characterized by more recent and gas-poor mergers. The stellar $V_{\text{rot}}/\sigma \sim 0.5$ would be consistent with a major merger of mass-ratio 1:3 (Bournaud et al. 2005). This gas-poor major merger would have likely occurred more recently, i.e. $z \lesssim 1$, and contributed to the accretion of a fraction of the ex-situ stars (Pulsoni et al. 2020). However, Proctor et al. (2005) found evidence of strong metallicity gradients in NGC 821, with the central regions showing young (~ 4 Gyr old) ages and high ($[Z/H] = 0.5$ dex) metallicities. Outside the central $1R_e$ of the galaxy, the ages steeply rise to ~ 12 Gyr and the metallicities drop to $\sim 1/3$ of the central value. These steep metallicity gradients rule out a recent major merger in the formation history of the galaxy that would produce a mixing of the stellar population and flatter metallicity gradients, as also shown with simulations (Cook et al. 2016). Therefore, it seems more likely that NGC 821 has experienced multiple minor mergers rather than a single major merger. Indeed, Bournaud et al. (2005) showed that multiple minor mergers in the mass-ratio range 1:4.5-1:10 have the same effect of a single major merger, ultimately producing an elliptical galaxy with hotter kinematics. For NGC 821, we, thus, propose that the galaxy formed through multiple gas-poor minor (at least two) mergers in the mass-ratio range 1:4.5-1:10 in more recent times (i.e. $z \lesssim 1$), similarly to NGC 4697. This formation scenario for NGC 821 would be in agreement with the conclusions reached by Proctor et al. (2005), who suggested that the most likely explanation for the central young and metal-rich stellar population in NGC 821 was the accretion of a low-mass galaxy that triggered a centrally concentrated burst of star formation from the in-situ gas of the galaxy. The decreasing V_{rot}/σ profile of the GCs (see Fig. 3) also suggests a minor merger scenario that is expected to produce little rotation of the GCs at larger radii (Bekki et al. 2005). Finally, the minor-axis rotation of the PNe at all radii as well as the kinematic misalignment shown by the GCs with respect to the underlying stars (see Fig. 3 and Appendix A6) could, possibly, be a result of the late gas-poor accretion history of NGC 821. Naab et al. (2014) found that late gas-poor major mergers can produce slowly rotating galaxies with kinematic twists and misalignment. In the case of NGC 821, the multiple (and late) gas-poor minor mergers could have had the effect of a gas-poor major merger, producing the minor-axis

rotation of the PNe. Coccato et al. (2009) found similar misalignment in the rotation velocity of the PNe with respect to the underlying stars and Pota et al. (2013) found that the blue GCs are rotating along the photometric minor-axis of the galaxy, consistently with the PNe, while some outer red GCs are counter-rotating with respect to the underlying stars. Coccato et al. (2009) suggested that the disagreement between the stars and PNe may be due to a rapid change of the major kinematic axis of rotation of NGC 821 just outside $\sim 1R_e$, beyond which the stellar kinematics do not reach. It would be interesting to extend the stellar kinematics beyond $1R_e$ with new observations in order to confirm whether the major kinematic axis of rotation of the stars changes beyond $\sim 1R_e$, in agreement with the PNe data.

NGC 4649 is the only cluster galaxy in our sample and the most massive together with NGC 5846. Therefore, NGC 4649 should be ex-situ dominated at all radii (Class IV galaxy; Pulsoni et al. 2020). This galaxy is expected to have had a very gas-poor accretion history, with only very small fraction of accreted gas (i.e. $< 20\%$), and to have experienced at least one gas-poor major merger in recent times, i.e. $z < 1$, that contributed to a large fraction (up to $\sim 40\%$) of the ex-situ stars (Pulsoni et al. 2020). Naab et al. (2014) found that a late gas-poor major merger can spin up the stars in the merger remnant, producing a fast rotator galaxy with rising λ_R profile out to $\sim 2R_e$, which roughly resembles the rising stellar V_{rot}/σ profile out to $\sim 2R_e$ of NGC 4649 in Fig. 3. According to Bournaud et al. (2005), a major merger with mass-ratio 1:3 can produce elliptical galaxies with less disk isophotes (low ellipticity) and stellar $V_{\text{rot}}/\sigma < 1$, which would also be consistent with our kinematic results in Fig. 3. Both the red and blue GCs sub-populations show rotation in the inner regions of the galaxy within $\sim 2R_e$, consistent with the photometric major-axis of the galaxy. The red GCs also show rotation at larger radii, i.e. beyond $\sim 4R_e$, which is overall aligned with the galaxy photometric major-axis (see Fig. 3). We note here that we do not detect rotation at large radii for the blue GCs, as for the red GCs, from our 1D kinematic profiles in Fig. 3. However, Pota et al. (2015) found that the blue GCs in NGC 4649 also show significant rotation at larger radii, similarly to the red GCs. However, Pota et al. (2015) found that the rotation of the blue GCs increases beyond $\sim 30\text{kpc}$. Our 1D kinematic profiles of NGC 4649 in Fig. 3 do not reach beyond $\sim 35\text{kpc}$, therefore we are not detecting the rotation of the blue GCs at larger radii. If the blue GCs are also rotating at larger radii as seen by Pota et al. (2015), then a late (i.e. $z < 1$) gas-poor major merger formation scenario would be consistent with the kinematic results shown in Fig. 3. In fact, according to Bekki et al. (2005), a major merger is expected to spin up both the red and blue GC sub-populations at larger radii, with the blue GCs having larger velocity dispersion than the red GCs, as we have seen in Fig. 3. We notice that the PNe also show a dip in the rotation velocity at $\sim 2R_e$, beyond which the rotation increases again but it is more closely aligned to the photometric minor-axis of the galaxy, as was also seen in Pota et al. (2015) and Coccato et al. (2013). The kinematic twist of the PNe could, possibly, also be a result of the late gas-poor major merger (Naab et al. 2014). Forbes et al. (2017a) have found a large number of ultra-compact dwarfs (UCDs) that are associated with NGC 4649. Strader et al. (2004) also identified a very massive UCD in NGC 4649, which is located at $\sim 2R_e$ towards

South-West, in correspondence of the rotation velocity dip of the PNe and red GCs (see Fig. 3). Therefore, these UCDs could be the remnant nuclei of dwarf galaxies (e.g. Drinkwater et al. 2000) that have been tidally stripped by NGC 4649 during its late (i.e. $z < 1$) gas-poor minor and mini merger accretion events that are expected to contribute in roughly equal amounts to the fraction of the ex-situ stars (Pulsoni et al. 2020).

Similarly to NGC 4649, NGC 5846 is also expected to be ex-situ dominated at all radii due to its large stellar mass. Therefore, its accretion history should be characterized by more very gas-poor merger events that happened very recently, i.e. $z < 1$. NGC 5846 is a massive slow rotator galaxy with $V_{\text{rot}}/\sigma \lesssim 0.2$ out to large radii, as seen from both the stars and PNe in Fig. 3. According to Naab et al. (2014)'s simulations, the kinematic properties of NGC 5846 would be more consistent with a formation history dominated by late gas-poor minor mergers, as a late gas-poor major merger is, instead, expected to produce a weakly rising stellar rotation out to $\sim 2R_e$. Indeed, multiple minor, as well as mini, mergers are expected to, ultimately, produce an elliptical slowly rotating galaxy, with similar properties as if it had undergone one single major merger (Bournaud et al. 2005). Finally, both the red and blue GC sub-populations do not show any strong rotation at large radii, consistent with a minor merger formation pathway (Bekki et al. 2005). We note here that the rotation of the red and blue GCs in the inner regions of the galaxy within $\sim 2-3R_e$ in Fig. 3 may not be real but due to the contamination of the GC system of NGC 5846 with outliers from its nearby companion galaxies, e.g. NGC 5846A, as also previously pointed out by Pota et al. (2013). We also mention this issue in the observed rotation of the red and blue GCs in the inner regions of NGC 5846 in Sec. A2.3.1. Therefore, we propose that NGC 5846 has likely formed through a series of multiple gas-poor minor mergers in recent times (i.e. $z < 1$), which may have also contributed ex-situ GCs.

5 SUMMARY AND CONCLUSIONS

In this work, we have studied the kinematic properties of 9 S0 and E/S0 galaxies (including NGC 3115 from Dolfi et al. 2020) by combining the stars from ATLAS^{3D} and SLUGGS with the discrete PNe and GC tracers, in order to probe the outer regions of the galaxies out to $\sim 4-6R_e$.

From 2D kinematic maps (see Fig. A1-A8) and 1D kinematic profiles (see Fig. 3), we find that:

- For NGC 1023, NGC 2768, NGC 3115, NGC 3377, NGC 4697 and NGC 7457 (*aligned* galaxies), the kinematics of their PNe and GC systems are well aligned with the kinematics of the stars in the overlapping radii. Overall, the rotation is also consistent with the photometric major-axis of the galaxies. This suggests that both the PNe and GC sub-populations are tracing the main underlying stellar population in these six galaxies out to large galactocentric radii;
- For NGC 821, NGC 4649 and NGC 5846 (*mis-aligned* galaxies), the kinematics of their PNe and GC systems are not aligned with the kinematics of the stars in the overlapping radii. Specifically, the PNe and GCs show rotation more closely aligned with the photometric minor-axis of the galaxy in NGC 821, while the PNe and blue GCs show a kinematic twist in the major-axis of rotation beyond $\sim 2R_e$ in NGC 4649

and, finally, no clear rotation is detected from all kinematic tracers in NGC 5846. This suggests more complex formation histories for these three galaxies that have likely involved more numerous and more recent mergers.

From the comparison with the simulations of Schulze et al. (2020), we suggest that four of the *aligned* galaxies (i.e. NGC 1023, NGC 3115, NGC 3377 and NGC 7457) show the characteristic *peaked* V_{rot}/σ profile shape, while the remaining two galaxies (i.e. NGC 2768 and NGC 4697) show the characteristic *flat* V_{rot}/σ profile shape. However, in Fig. 4, we see that all six *aligned* galaxies show similar kinematic behaviours at large radii, i.e. beyond $\sim 2\text{--}3R_e$, characterized by low V_{rot}/σ . Therefore, we suggest two main times in the assembly history of the six *aligned* galaxies. At late ($z \lesssim 1$) times, all six *aligned* galaxies had similar accretion histories likely characterized by the accretion of dwarf galaxies in mini mergers that enhanced the velocity dispersion of the galaxies in the outer regions (i.e. beyond $\sim 2\text{--}3R_e$) without altering their central disk-like kinematics. However, from the differences in the V_{rot}/σ profiles of the galaxies in the central regions (i.e. within $\sim 2\text{--}3R_e$), we suggest that the two *flat* galaxies had, possibly, experienced also a late ($z \lesssim 1$), and relatively more gas-poor, minor merger that flattened the V_{rot}/σ profile in the central regions of the galaxy (Schulze et al. 2020; Pulsoni et al. 2020). On the other hand, we suggest that the four galaxies with *peaked* V_{rot}/σ profiles had, possibly, experienced an early ($z > 1$) gas-rich minor merger with some larger accreted gas fractions that preserved the amplitude of the V_{rot}/σ peak in the central regions of the galaxies (Pulsoni et al. 2020), or had evolved mostly passively through secular evolution as it seems to be the case for NGC 7457.

Among the four *peaked* galaxies, we also note differences in the 1D kinematic profiles of their tracers (see Fig. 3), therefore suggesting differences in their individual assembly histories that in some cases may, possibly, be a result of the specific orbital configuration of the mergers (see Sec. 4.2.1). Specifically, we suggest that the orbital configuration of the minor and mini merger events may have induced the formation of the bar in NGC 1023, i.e. a minor merger of mass-ratio 1:10 with closely aligned spin angles (Cavanagh & Bekki 2020), as well as the higher rotation velocity amplitude of the blue GCs than the red GCs at $\sim 3R_e$ in NGC 3115 (Bekki et al. 2005). In fact, the late accretion of low-mass dwarf galaxies along a preferential direction may have caused the more extended disk-like kinematics in NGC 3115 than in NGC 1023, i.e. mini mergers occurring along the disk plane of the galaxy (Karademir et al. 2019). However, further simulations of GC kinematics that explore a wider range of parameters in the orbital configuration of the mergers would be required in order to explain these observed differences.

Finally, all three *mis-aligned* galaxies had also overall similar assembly histories, characterized by late (i.e. $z < 1$) mergers. These mergers were likely minor and occurred more than once in the case of NGC 821 and NGC 5846, therefore enhancing the velocity dispersion of the kinematic tracers at all radii. On the other hand, NGC 4649 is likely the result of a major merger (i.e. mass-ratio $> 1:4$) that spun-up both the red and blue GC sub-populations at large radii, with minor and mini merger events that contributed to its population of ultra compact dwarfs (UCDs).

In this work, we find that the formation histories of S0

galaxies in low-density environments can be quite complex with merger events playing a crucial role in shaping the observed distinct V_{rot}/σ profiles of the different kinematic tracers in our galaxies out to large radii, depending mainly on their time of occurrence, specific orbital configuration and mass-ratio.

ACKNOWLEDGEMENTS

We thank the anonymous referee for their very constructive comments and suggestions that helped improving this paper. We thank the SLUGGS team for the collection, reduction and initial analysis of data from the SLUGGS survey used in this paper. We would like to thank Adebisola Alabi for providing the spectroscopic PNe catalogues of some of the galaxies studied in this work. We thank Michael Drinkwater for useful discussions that have helped to improve this paper. DF, WC, KB and AD acknowledge support from the Australian Research Council under Discovery Project 170102344. AFM has received financial support through the Postdoctoral Junior Leader Fellowship Programme from ‘La Caixa’ Banking Foundation (LCF/BQ/LI18/11630007). AJR was supported by National Science Foundation grant AST-1616710 and as a Research Corporation for Science Advancement Cottrell Scholar.

DATA AVAILABILITY

Original Keck data are available from the Keck Observatory Archive (<https://www2.keck.hawaii.edu/koa/public/koa.php>).

APPENDIX A: DESCRIPTION OF THE INDIVIDUAL GALAXIES

In this section, we describe in more details the main properties and kinematic features of each individual galaxy listed in Table 1. As previously mentioned in Sec. 2, all galaxies listed in Table 1 show evidence of a rotating disk-like component from early studies. Apart from NGC 1023, NGC 3115 and NGC 7457 that are morphologically classified as S0s (see Table 1), NGC 821 shows evidence of a rapidly rotating stellar disk (Emsellem et al. 2004; Proctor et al. 2009), whose presence was also suggested from early photometric studies (e.g. Michard & Marchal 1994; Goudfrooij et al. 1994; Ravindranath et al. 2001) as well as from stellar population studies (Proctor et al. 2005). Similarly, evidence of a rotating stellar disk was also found in NGC 2768 (e.g. Forbes et al. 2012), NGC 3377 (Halliday et al. 2001) and NGC 4697 (Spiniello et al. 2015; Foster et al. 2016) from stellar kinematic or population studies. The presence of a disk is not clear in NGC 4649 (Pota et al. 2015) or in NGC 5846, which has conflicting morphological classification (i.e. E0-1 in RC2 and S0 in RSA; Michard & Marchal 1994). Therefore, apart from these two not clearly defined galaxies (i.e. NGC 4649 and NGC 5846), all our selected ETGs in Table 1 show evidence of a disk-like component, supporting our choice of including them in this current study of the assembly history of S0 galaxies.

The description of the kinematic results of all the distinct tracers (i.e. stars, PNe and GC sub-populations) for each

galaxy is based on the 2D kinematic maps and 1D kinematic profiles shown in Fig. 2 and A1-A8 and in Fig. 3, respectively, that are obtained as described in Sec. 3.1. We describe separately the *aligned* and *mis-aligned* galaxies introduced in Sec. 3.2.

A1 Aligned galaxies

A1.1 NGC 1023

NGC 1023 is the brightest member of a small galaxy group in Perseus (namely the NGC 1023 group), which is composed of 13 bound galaxies (Tully 1980). Specifically, NGC 1023 is classified as an SB0 galaxy from early photometric studies that confirmed the presence of a barred bulge (e.g. Barbon & Capaccioli 1975), which is found to rotate rapidly (Kormendy 1982). NGC 1023 has also a companion dwarf satellite galaxy, NGC 1023A, located South-East of its nucleus (see figure 2 of Barbon & Capaccioli 1975). The possible interaction between these two systems has been discussed in the literature as a potential explanation for the origin and peculiar distribution of the neutral hydrogen HI mass cloud observed around NGC 1023 (Sancisi et al. 1984; Capaccioli et al. 1986).

The GC system contains 110 objects, six of which are likely associated with the nearby dwarf galaxy NGC 1023A (Cortesi et al. 2016). Cortesi et al. (2016) also removed some additional GCs that deviate strongly from the general rotation pattern of NGC 1023, however we choose to only remove two of these GCs (both are blue) that strongly counter-rotate at $\sim 2R_e$. The final GC catalogue contains 102 objects that display a clear colour-bimodality distribution for $(g-z) = 1.13$. Therefore, we split between the red, metal-rich and blue, metal-poor GC sub-populations that contain 41 and 61 objects, respectively.

The PNe system is publicly available in Noordermeer et al. (2008) and it contains 203 PNe, twenty of which are likely to belong to the nearby NGC 1023A dwarf galaxy (Noordermeer et al. 2008). After excluding this group of 20 PNe, we obtain a final sample of 183 PNe for NGC 1023.

A1.1.1 Kinematic profiles

NGC 1023 is characterized by an increasing stellar rotation velocity profile from the innermost regions within $\sim 0.5R_e$ (ATLAS^{3D}) out to $\sim 1R_e$, beyond which the rotation remains roughly constant out to $\sim 2R_e$. There is, possibly, evidence that the stellar rotation velocity starts decreasing beyond $\sim 2R_e$ (see Fig.3). The rotation velocity profile of the PNe shows excellent agreement with that of the stars in the overlapping radii between $\sim 1-2.5R_e$. At larger radii (i.e. beyond $\sim 2R_e$), the PNe rotation velocity decreases out to $\sim 5R_e$. The red and blue GC sub-populations show decreasing rotation velocity profiles out to $\sim 3.5R_e$ and $\sim 5.5R_e$, respectively, which are overall consistent within the 1-sigma errors. We see that the red GC rotation velocity profile is also consistent with both that of the stars and PNe, with similar amplitude at $\sim 1.5R_e$. On the other hand, the blue GC rotation velocity profile has somewhat smaller amplitude than the stars, PNe and red GCs at $\sim 2R_e$, while it shows good agreement with the PNe and red GCs at larger radii. Cortesi et al. (2016) found that the blue GCs also display strong rotation velocity within the inner $\sim 2.5R_e$, with similar amplitude to that of the stars, PNe and red GCs. We argue that the observed difference between

our rotation velocity profile of the blue GCs with respect to that in Cortesi et al. (2016) at $\sim 2R_e$ may be the result of the removal of additional blue GCs deviating strongly from the regular rotation pattern of NGC 1023, as well as of the larger elliptical annuli used in Cortesi et al. (2016) than in this work to derive the corresponding 1D kinematic profiles.

The stellar velocity dispersion profile peaks at $\sim 200\text{km s}^{-1}$ within $\sim 0.5R_e$ (ATLAS^{3D}) and, subsequently, steeply decreases out to $\sim 1R_e$, beyond which it remains roughly constant to $\lesssim 100\text{km s}^{-1}$ out to $\sim 2R_e$. The small region with very low ($\sim 20\text{km s}^{-1}$) velocity dispersion, seen at $\sim 3R_e$ towards South-East in Fig. 2, is likely associated with the presence of the companion galaxy, NGC 1023A, given the closely overlapping spatial locations (e.g. Cortesi et al. 2016). The PNe show a weakly increasing velocity dispersion profile as a function of galactocentric radius, with higher values displayed at larger radii beyond $\sim 2R_e$. The red and blue GC sub-populations have similar increasing velocity dispersion profiles as a function of galactocentric radius, consistent with that of the PNe within the 1-sigma errors. This increasing behaviour of the velocity dispersion profiles of the PNe, red and blue GCs was also previously observed in Cortesi et al. (2016).

The stellar V_{rot}/σ profile rises steeply to $V_{\text{rot}}/\sigma \sim 3$ within the inner $\sim 1R_e$ and, then, it remains roughly flat out to $\sim 2.5R_e$. Similarly, the PNe show high values of the $V_{\text{rot}}/\sigma \sim 2$ between $\sim 1-2R_e$, consistent with the stars within the 1-sigma errors. At larger radii, the V_{rot}/σ profile of the PNe decreases down to values $\lesssim 1$ out to $\sim 5R_e$. The red and blue GCs show decreasing V_{rot}/σ profiles out to large radii, overall consistent with that of the PNe within the 1-sigma errors. The red GCs show similar $V_{\text{rot}}/\sigma \sim 2$ amplitude to the PNe at $\sim 1.5R_e$, while the blue GCs have lower $V_{\text{rot}}/\sigma \sim 1$ than the PNe at $\sim 2R_e$, but consistent with the red GCs within the 1-sigma errors.

The PA_{kin} profiles show good kinematic alignment between the stars, PNe, red and blue GC sub-populations, which are all consistent with rotation along the photometric major-axis of the galaxy at all radii within the 1-sigma errors. The q_{kin} profile of the stars shows that the inner regions within $\sim 0.5R_e$ are characterized by lower ellipticity (high q_{kin}) than the outer regions of the galaxy beyond $\sim 0.5R_e$, where the ellipticity is consistent with the photometric value out to $\sim 2.5R_e$.

A1.2 NGC 2768

NGC 2768 is classified as an E6/S0 group galaxy (Sandage & Bedke 1994). This galaxy is found to be characterized by red colours with a dust lane running along its photometric minor axis (Kim 1989). Ionized gas has also been detected within $\sim 20''$ from the central regions of the galaxy (Kim 1989), and, interestingly, this gas is found to be kinematically misaligned with respect to the stars due to its rotation along the photometric minor-axis of the galaxy (Wiklind & Henkel 1995; Sarzi et al. 2006).

The GC system contains 109 objects, displaying a clear colour bimodality distribution for $(g-i) \sim 1.02$ (Pota et al. 2013). Adopting this colour-split, we identify 37 red, metal-rich and 44 blue, metal-poor GCs. The PNe system is publicly available in Cortesi et al. (2013b) and it contains 315 PNe.

The stellar, GC and PNe kinematics of NGC 2768 were previously studied by Forbes et al. (2012), who found overall good agreement between the kinematic profiles of the distinct

tracers and significant rotation for the disk component of the galaxy with rising V_{rot}/σ profile out to $\sim 4R_e$. A similar rising trend was also found for the V_{rot} profile of the PNe by [Zanatta et al. \(2018\)](#). However, they found that both the red and blue GC sub-populations display lower amount of rotation, more consistent with spheroid-like kinematics.

A1.2.1 Kinematic profiles

NGC 2768 is characterized by an increasing stellar rotation velocity profile out to $\sim 2R_e$. We find a rotation amplitude offset of $\sim 40\text{--}50\text{km s}^{-1}$ between ATLAS^{3D} and SLUGGS at $\sim 0.4R_e$, with ATLAS^{3D} showing a steeper increase of the rotation velocity than SLUGGS. On the other hand, the stellar velocity dispersion profile does not show any offset at $\sim 0.4R_e$ and is continuously decreasing out to $\sim 2R_e$.

The PNe show rotation velocity consistent with the stars out to $\sim 2R_e$ along the photometric major-axis of the galaxy, with a peak in the rotation velocity between $\sim 1.2\text{--}1.4R_e$ and a subsequent small dip between $\sim 2\text{--}3R_e$. Beyond this radius, the rotation velocity profile of the PNe smoothly increases again out to $\sim 6R_e$. Clear rotation is also seen for both the red and blue GC sub-populations between $\sim 1\text{--}3R_e$ along the photometric major-axis of the galaxy, similarly to the stars and PNe. The red GCs show a slightly decreasing rotation velocity profile out to $\sim 3R_e$, consistent with the PNe. The blue GCs also show a decreasing rotation velocity profile out to $\sim 2.5R_e$, beyond which it remains constant out to $\sim 4R_e$. Overall, the PNe, red and blue GC rotation velocity profiles are consistent with each other within the 1-sigma errors out to $\sim 3R_e$. They also show consistency with the rotation velocity of the stars at $\sim 1.5R_e$, but we are unable to confirm the kinematic agreement beyond this radius due to the limited extension of the SLUGGS stellar kinematic data.

The velocity dispersion profiles of the PNe, red and blue GCs are consistent with each other within the 1-sigma errors and show smoothly decreasing trends out to large radii along the photometric major-axis of the galaxy. From the 2D kinematic maps in Fig. A1, we see that the velocity dispersion of the PNe, red and blue GCs show higher values along the photometric minor-axis of the galaxy. They also show consistency with the stellar velocity dispersion profile at $\sim 1.5R_e$, but, as for the rotation velocity, we are unable to confirm this at larger radii.

The stellar V_{rot}/σ profile rises up to ~ 1.5 within $2R_e$. The PNe and red GCs show similar $V_{\text{rot}}/\sigma \sim 1$ profiles, which remains roughly flat and are consistent with the stars at $\sim 1.5R_e$. The blue GCs show a decreasing V_{rot}/σ profile out to $\sim 2.5R_e$, beyond which it remains overall flat out to large radii and consistent with the V_{rot}/σ profiles of both the PNe and red GCs within the 1-sigma errors.

The PA_{kin} profiles show that the stars, PNe, red and blue GCs are kinematically aligned and are rotating along the photometric major-axis of the galaxy at all radii. The q_{kin} profile of the stars is consistent with the photometric value within the inner $\sim 0.5R_e$, while it decreases out to $\sim 2R_e$. The q_{kin} profile of the red GCs is consistent with that of the stars between $\sim 1\text{--}2R_e$ and it increases up to the photometric value at larger radii. However, we note that the q_{kin} profile of the red GCs is overall consistent with the photometric value at all radii within the 1-sigma errors.

A1.3 NGC 3377

NGC 3377 is a bright elliptical galaxy of E5-6 morphological type ([Sandage & Tammann 1987](#)), characterized by a small disk embedded in a boxy halo ([Halliday et al. 2001](#)). This galaxy is a member of the Leo I group with the smaller NGC 3377A being its nearest companion galaxy.

The GC system contains 126 objects, characterized by a bimodal colour distribution as was already found by [Pota et al. \(2013\)](#). We study the kinematics of 46 red, metal-rich and 80 blue, metal-poor GCs adopting the colour-split ($g - i$) = 0.925.

The PNe system contains 152 objects. The PNe kinematics for this galaxy were initially studied by [Coccato et al. \(2009\)](#), who found significant rotation in the inner regions of the galaxy, i.e. within $\sim 100''$, which is characterized by a twist in the kinematic position angle (PA_{kin}) between $60''$ and $200''$.

A1.3.1 Kinematic profiles

NGC 3377 shows roughly constant ($\sim 80\text{--}100\text{km s}^{-1}$) stellar rotation velocity out to $\sim 1R_e$, followed by a subsequent decrease out to $\sim 2\text{--}2.5R_e$. ATLAS^{3D} has shown that the stellar rotation velocity is also high in the central $\sim 0.5R_e$, consistent with the SLUGGS stellar kinematics. The PNe also show a decreasing rotation velocity profile out to $\sim 2\text{--}3R_e$, which is overall consistent with that of the stars within $\sim 1\text{--}2R_e$ despite an offset of $\sim 40\text{--}50\text{km s}^{-1}$ at $\sim 1R_e$. At larger radii, i.e. beyond $\sim 3R_e$, the rotation velocity of the PNe shows evidence of slightly increasing again towards North (see Fig. A2), where the rotation, possibly, occurs along a different PA_{kin} than that of the inner $\sim 2R_e$ (see Fig. 3). The red GCs show decreasing rotation velocity profile out to $\sim 3R_e$, which is consistent with both that of the stars and PNe in the overlapping radii. Some red GCs seem to be rotating along the galaxy photometric minor-axis between $\sim 3\text{--}4R_e$ towards South-East (see Fig. A2). On the other hand, the blue GCs do not show evidence of any clear rotation at all radii.

The stellar velocity dispersion profile slightly increases from ~ 80 to $\sim 100\text{km s}^{-1}$ between $\sim 1\text{--}2.5R_e$. This behaviour is likely mimicking the increase of the stellar velocity dispersion at large radii, moving away from the photometric major-axis of the galaxy where the rotating disk-like structure is observed, as seen from the 2D kinematic map in Fig. A2 and also previously shown by [Foster et al. \(2016\)](#). ATLAS^{3D} also show consistent results, with lower velocity dispersion along the photometric major-axis of the galaxy. However, ATLAS^{3D} shows higher velocity dispersion within $\sim 0.5R_e$ with an offset of $\sim 20\text{km s}^{-1}$ from SLUGGS at $\sim 1R_e$. The PNe and red GCs show very consistent, and decreasing, velocity dispersion profiles between $\sim 2\text{--}3R_e$. At larger radii, the velocity dispersion profile of the PNe remains roughly constant out to $\sim 6R_e$. The blue GCs also show decreasing velocity dispersion profile between $\sim 2\text{--}3R_e$, consistent with the PNe and red GCs, beyond which it remains roughly constant out to $\sim 6R_e$. The blue GCs show higher velocity dispersion along the photometric minor-axis of the galaxy, similarly to the stars (see Fig. A2). Overall, the velocity dispersion profiles of the PNe, red and blue GCs also show consistency with that of the stars in the overlapping radii at $\sim 2R_e$, but we are unable to confirm such agreement at larger radii due to the limited extension of the stellar kinematic data.

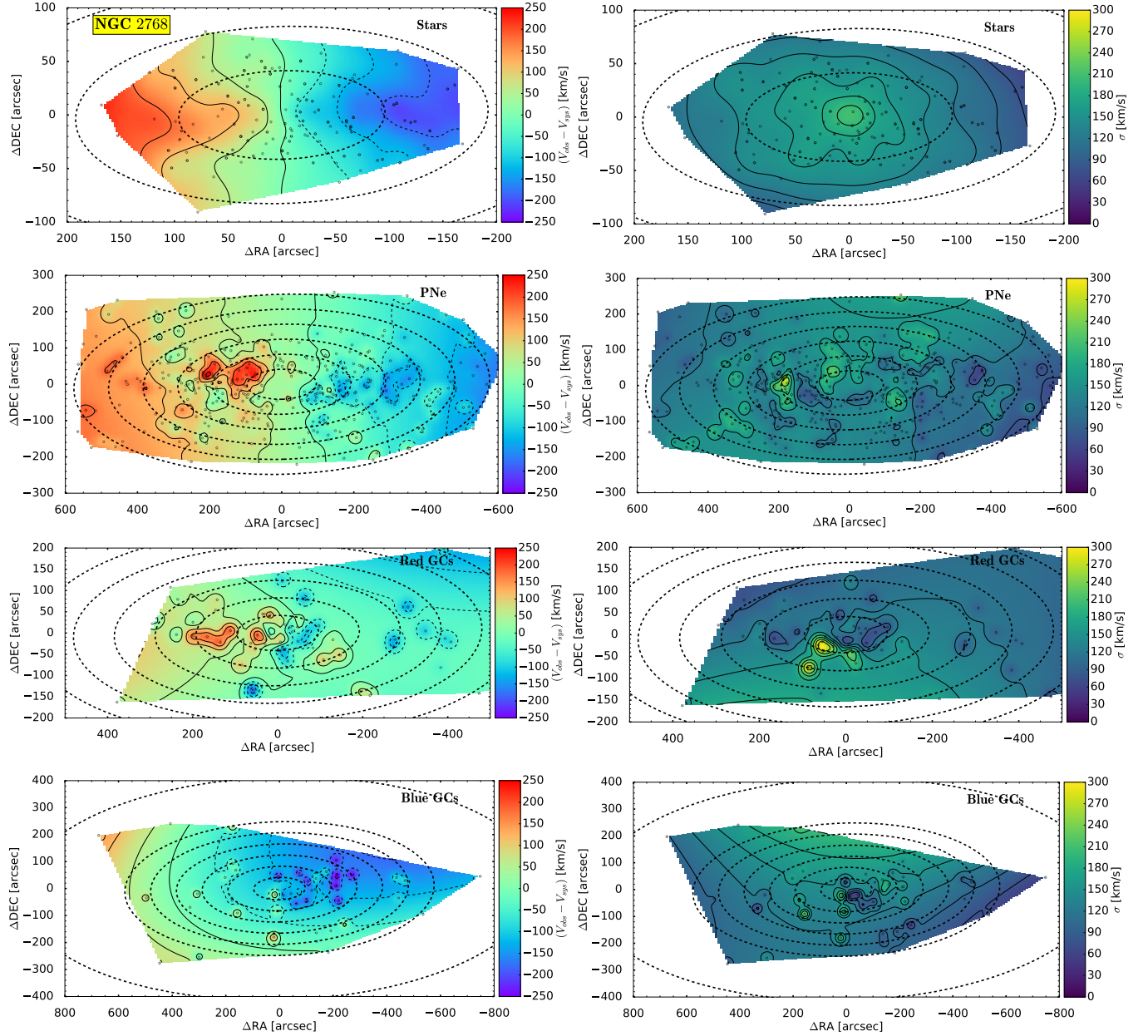


Figure A1. From top to bottom, 2D velocity (left-hand side) and velocity dispersion (right-hand side) maps of the SLUGGS stars, PNe, red and blue GCs for NGC 2768. The description is as in Fig. 2.

The stellar V_{rot}/σ profile steeply decreases between $\sim 1-2R_e$. The PNe show a similar decreasing V_{rot}/σ profile out to large radii, i.e. $\sim 5R_e$, which is consistent with that of the stars in the overlapping radii within $\sim 2R_e$. The red GCs also show a smoothly decreasing V_{rot}/σ profile, consistent with both that of the stars and PNe. On the other hand, the blue GCs are not rotating, with $V_{\text{rot}}/\sigma < 0.5$ at all radii.

The PA_{kin} profile of the PNe shows that the rotation is overall kinematically aligned with that of the stars along the photometric major-axis of the galaxy within $\sim 3R_e$. At larger radii, i.e. between $\sim 3-5R_e$, we see a twist of the PA_{kin} , which shows rotation along an $\sim 180^\circ$ kinematic position angle. We have seen this, possible, twist of the kinematic axis of rotation of the PNe beyond $\sim 3R_e$ in the 2D kinematic maps of Fig.

A2 and it was also previously shown in [Coccato et al. \(2009\)](#). The q_{kin} profile of the stars is roughly constant at all radii and consistent with the photometric value.

A1.4 NGC 4697

NGC 4697 is a disk elliptical galaxy classified as E6 ([Michard & Marchal 1994](#)), which belongs to a galaxy group located in the Virgo Southern Extension ([Blakeslee et al. 2009](#)). Stellar kinematic studies have classified this galaxy as a fast-rotator (e.g. [Spiniello et al. 2015](#); [Foster et al. 2016](#)), while stellar population analyses have found an older and metal-poorer stellar population in the bulge than in the disk ([Spiniello et al. 2015](#)).

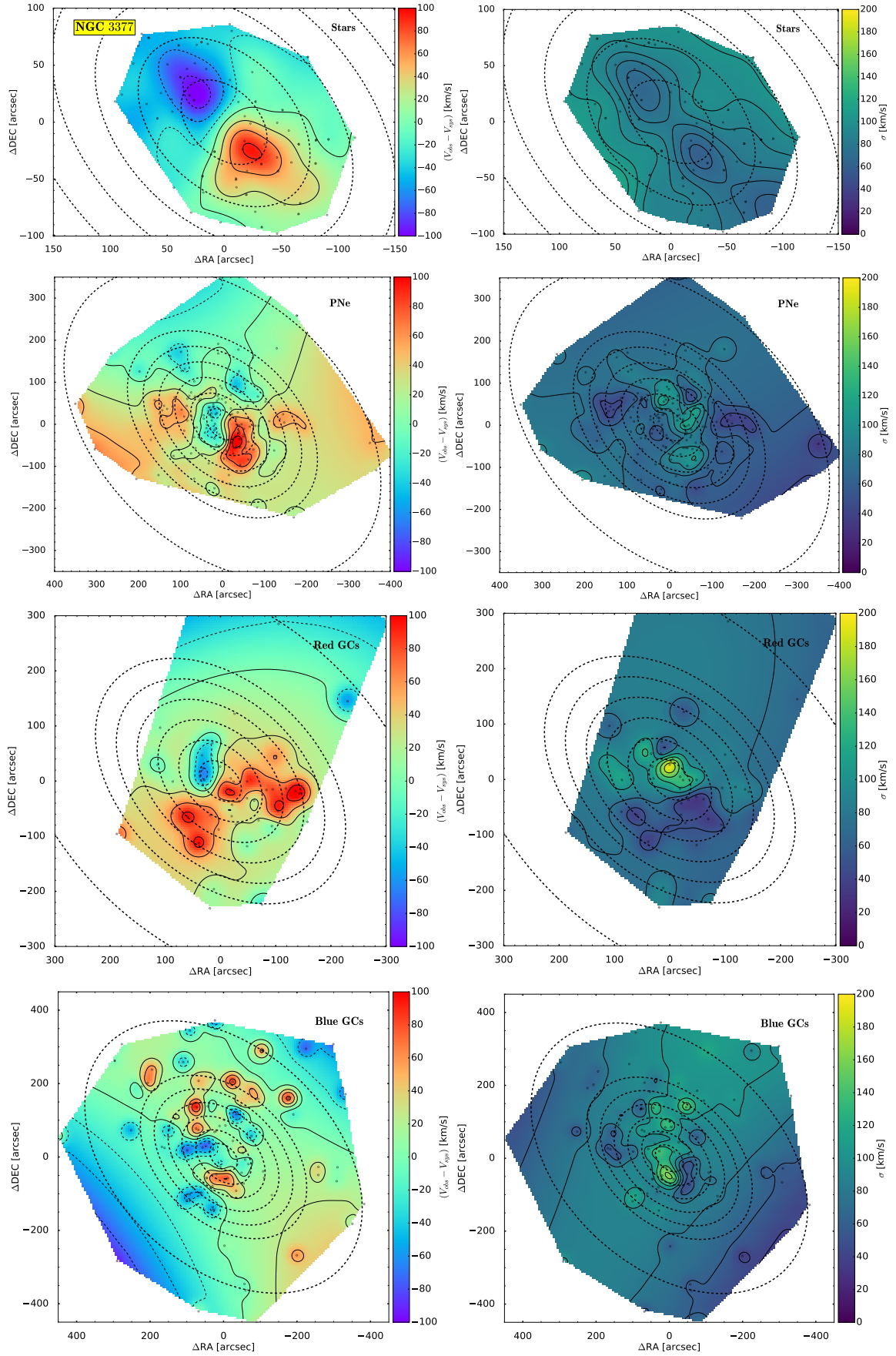


Figure A2. From top to bottom, 2D velocity (left-hand side) and velocity dispersion (right-hand side) maps of the SLUGGS stars, PNe, red and blue GCs for NGC 3377. The description is as in Fig. 2.

The GC system of NGC 4697 contains 86 spectroscopically confirmed objects. We do not find evidence of any clear colour bimodality in the GC population, therefore we do not split between the two red, metal-rich and blue, metal-poor GC sub-populations for studying the GC kinematics of this galaxy.

The PNe system of NGC 4697 is publicly available in [Méndez et al. \(2001, 2008\)](#) and it contains a total of 531 objects. The kinematics of the PNe system were studied by [Coccato et al. \(2009\)](#), who found evidence of rotation within $\sim 1R_e$ along the photometric major-axis consistent with the stars. In a previous work, [Sambhus et al. \(2006\)](#) studied a PNe sub-sample containing 320 objects, defined by all PNe with apparent magnitudes brighter than $[OIII](\lambda = 5007\text{\AA}) = 27.6\text{mag}$ outside a central elliptical region with semi-major axis length $a = 60''$ ([Méndez et al. 2001](#)). They found a correlation between the PNe velocities and their $[OIII](\lambda = 5007\text{\AA})$ magnitudes, with faint PNe displaying co-rotation and bright PNe (i.e. $[OIII](\lambda = 5007\text{\AA}) < 26.2\text{mag}$) counter-rotation.

Therefore, [Sambhus et al. \(2006\)](#) studied separately the faint (i.e. $[OIII](\lambda = 5007\text{\AA}) > 26.9\text{mag}$), intermediate (i.e. $26.2\text{mag} < [OIII](\lambda = 5007\text{\AA}) < 26.9\text{mag}$) and bright (i.e. $[OIII](\lambda = 5007\text{\AA}) < 26.2\text{mag}$) PNe sub-populations, where the magnitude cuts were chosen to have equal-width bins with $\Delta[OIII](\lambda = 5007\text{\AA}) = 0.7\text{mag}$. The azimuthal distributions of the bright and faint PNe sub-populations were only found to have 2% probabilities of being consistent, while the intermediate and faint PNe were more consistent with a 28% probability and the intermediate and bright PNe were only consistent with a 7% probability from the Kolmogorov-Smirnov (KS) test.

We consider the PNe catalogue of 526 objects with both radial velocity and magnitude measurements, and we compare the PNe velocities with respect to the underlying 2D stellar velocity field. For the comparison, we use the 2D stellar kinematics from the SLUGGS survey ([Arnold et al. 2014; Foster et al. 2016](#)). The aim is to test whether the PNe show a significantly different kinematic behaviour with respect to the underlying stars and, if that is the case, whether such different behaviour shows any dependance as a function of the PNe apparent magnitudes, $[OIII](\lambda = 5007\text{\AA})$.

Therefore, we calculate the PNe velocities and velocity dispersion relative to the underlying 2D stellar velocity field at the PNe location, i.e. $(V_{PNe} - V_{stars})$ and $(\sigma_{PNe} - \sigma_{stars})$, as a function of the apparent PNe magnitudes, $[OIII](\lambda = 5007\text{\AA})$. Here, V_{PNe} refers to the PNe velocity already subtracted by the V_{sys} of NGC 4697 and the velocity dispersion is estimated at the location of each PNe from the standard deviation of the PNe velocities in bins containing the 10 nearest objects. We use all 526 PNe in the catalogue and we calculate the average velocities and velocity dispersion in magnitude bins containing 30 objects.

We find that there is a large scatter of the PNe velocities and velocity dispersion relatively to the underlying 2D stellar velocity and velocity dispersion fields. However we do not find evidence of a strong trend of the PNe velocities and velocity dispersion as a function of the PNe magnitudes, $[OIII](\lambda = 5007\text{\AA})$, which are overall consistent with the underlying stellar kinematics. Therefore, based on these results, we choose not to split the PNe catalogue of NGC 4697 into the magnitude bins adopted in [Sambhus et al. \(2006\)](#), but we will study the kinematics of the PNe population as a whole.

A1.4.1 Kinematic profiles

NGC 4697 shows a smoothly decreasing stellar rotation velocity profile out to $\sim 2.5R_e$. The ATLAS^{3D} and SLUGGS stellar rotation velocity profiles are consistent with each other, despite the offset in rotation of $\sim 20\text{kms}^{-1}$ at $\sim 0.5R_e$. The PNe and GCs show consistent rotation velocity profiles, with a peak of rotation occurring at $\sim 1R_e$ and a subsequent sharp decrease out to $\sim 1.5-2R_e$, beyond which the rotation velocity remains roughly constant out to $\sim 3.5R_e$. Some GCs show evidence of counter-rotation at $\sim 2R_e$ towards South-West as seen in Fig. A3.

The stellar velocity dispersion smoothly decreases out to $\sim 2.5R_e$ along the photometric major-axis of the galaxy, while it remains roughly constant along the photometric minor-axis of the galaxy (see Fig. A3). The PNe show a similar decreasing velocity dispersion behaviour, as the stars, out to $\sim 3.5R_e$ along the photometric major-axis of the galaxy. On the other hand, the GCs have a roughly constant velocity dispersion profile at all radii, whose amplitude is consistent with that of the stars and PNe beyond $\sim 2R_e$.

The stellar $V_{rot}/\sigma \sim 0.5$ profile remains roughly flat out to large radii, i.e. $\sim 2.5R_e$. The PNe and GCs have consistent V_{rot}/σ profiles, with a peak at $\sim 1R_e$ and a subsequent sharp decrease out to large radii, similarly to the behaviour of the corresponding V_{rot} profiles.

The PA_{kin} profiles show good kinematic alignment between the stars and PNe out to $\sim 2.5R_e$, with the rotation occurring along the photometric major-axis of the galaxy. Beyond $\sim 2.5R_e$, the PNe, possibly, show some kinematic misalignment from the photometric major-axis, but they are overall consistent with it within the 1-sigma errors. Additionally, we do not clearly see evidence of a possible kinematic misalignment beyond $\sim 2.5R_e$ from the 2D kinematic maps in Fig. A3. The q_{kin} profile of the stars is roughly constant at all radii out to $\sim 2.5R_e$ and lower than the photometric value, implying higher flattening for the stars.

A1.5 NGC 7457

NGC 7457 is a disk-dominated S0 galaxy found in isolation with the possible evidence of a bar-like structure ([Michard & Marchal 1994](#)). Early studies have identified the presence of a small, compact nucleus within the innermost galaxy regions with a young ($\sim 2-2.5\text{Gyr}$ old) stellar population, which displays counter-rotation with respect to the galaxy bulge and disk ([Sil'chenko et al. 2002](#)). Evidence for a kinematically distinct core (KDC) characterized by young stellar ages in NGC 7457 has been also found by [Kuntschner et al. \(2006, 2010\)](#), who measured a strong $H\beta$ absorption.

The GC system of NGC 7457 contains 40 objects without evidence of any color bi-modality distribution. Therefore, we do not adopt any colour-split to separate between the two red, metal-rich and blue, metal-poor GC sub-populations.

The PNe system of NGC 7457 contains 113 objects. The combined kinematics of both the PNe and GC systems of NGC 7457 were previously studied by [Zanatta et al. \(2018\)](#), who found this galaxy to be rotationally supported with $V_{rot}/\sigma > 2$ at all radii.

A1.5.1 Kinematic profiles

NGC 7457 shows an increasing stellar rotation velocity profile out to $\sim 2R_e$. Such behaviour is observed from both ATLAS^{3D}

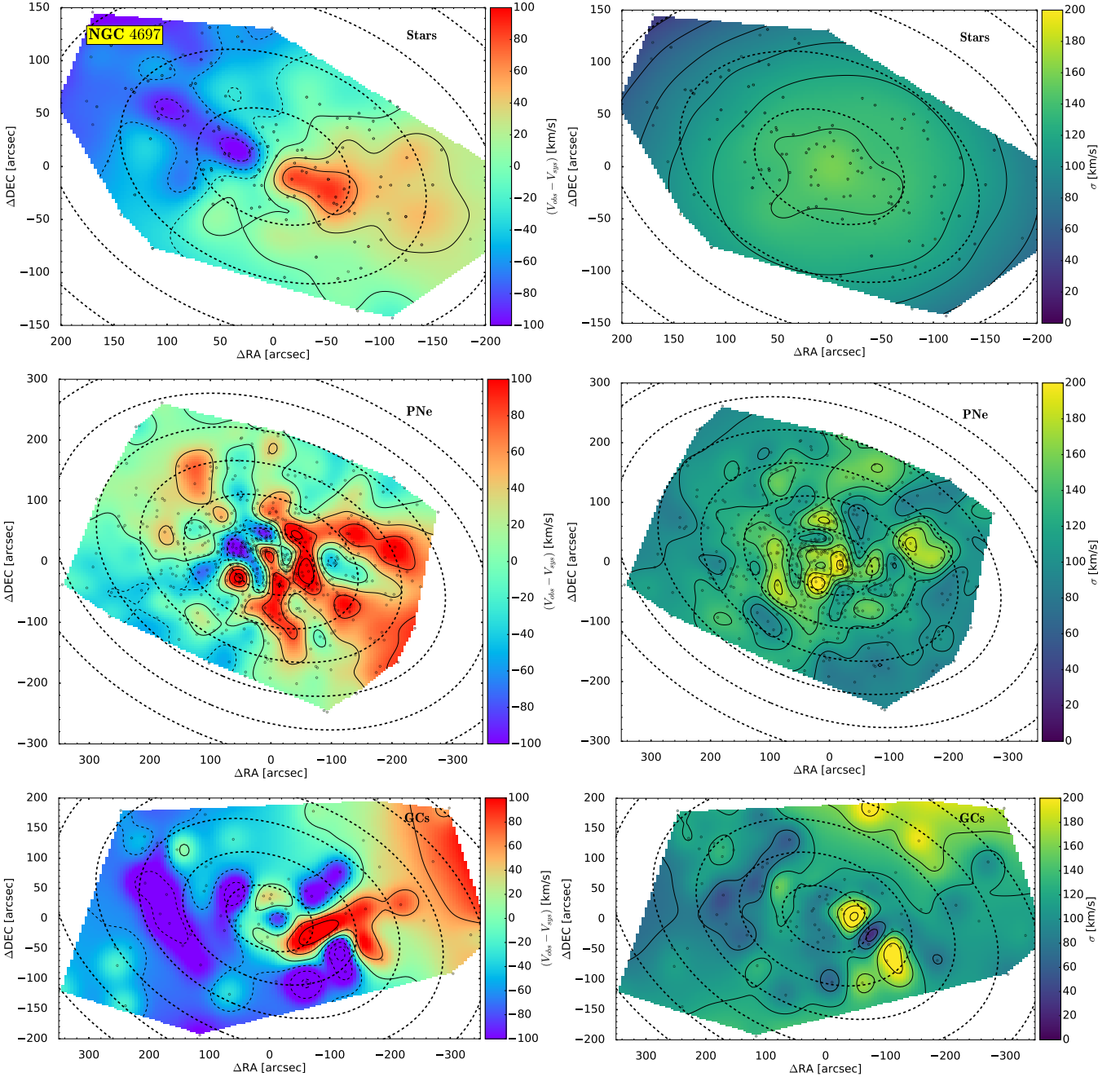


Figure A3. From top to bottom, 2D velocity (left-hand side) and velocity dispersion (right-hand side) maps of the SLUGGS stars, PNe and GCs for NGC 4697. The description is as in Fig. 2.

(within $\sim 0.5R_e$) and SLUGGS, which show good agreement in the rotation velocity. Both PNe and GCs also show a rising rotation velocity profile out to $\sim 2R_e$, very consistent with the stars. Beyond $\sim 2R_e$, the rotation velocity profile of the GCs shows evidence of starting to decrease (see Fig. 3).

The stellar velocity dispersion from SLUGGS is very low (i.e. $\sim 30\text{--}45\text{ km s}^{-1}$) at all radii with, possibly, a mild central peak of $\sim 45\text{--}50\text{ km s}^{-1}$ (see Fig. A4), as previously shown by Foster et al. (2016) and Bellstedt et al. (2017). The stellar velocity dispersion from ATLAS^{3D} shows inconsistency with SLUGGS in the inner $\sim 0.5R_e$, being characterized by higher values of $\sim 75\text{ km s}^{-1}$, as also previously shown in Bellstedt

et al. (2017). It is not clear what causes this offset. The velocity dispersion of the PNe and GCs are higher than that of the stars in some localized regions, mostly along the photometric minor-axis of the galaxy (see Fig. A4). However, the velocity dispersion profiles of the PNe and GCs are overall very consistent with each other, as well as with that of the stars, within the 1-sigma errors and show very low (i.e. $\sim 40\text{ km s}^{-1}$) values at all radii (see Fig. 3).

The V_{rot}/σ profiles of the stars, PNe and GCs are very consistent with each other, rising up to $V_{\text{rot}}/\sigma \sim 2\text{--}3$ within $\sim 2\text{--}2.5R_e$.

The PA_{kin} profiles show good kinematic alignment between

the stars, PNe and GCs, which are rotating along the photometric major-axis of the galaxy at all radii. The q_{kin} profile of the stars is consistent with the photometric value of the galaxy between $\sim 0.5-2R_e$, while it is higher (low ellipticity) in the central regions within $\sim 0.5R_e$.

A2 Mis-aligned galaxies

A2.1 NGC 821

NGC 821 is an isolated elliptical galaxy classified as E6 according to NED³. However, [Emsellem et al. \(2004\)](#) found evidence of a rapidly rotating disk-like component from stellar kinematic studies, as part of the SAURON project. Further evidence of the presence of a stellar disk in NGC 821 comes also from earlier photometric studies, e.g. [Michard & Marchal \(1994\)](#); [Goudfrooij et al. \(1994\)](#); [Ravindranath et al. \(2001\)](#) as well as from stellar population and kinematic studies ([Proctor et al. 2005, 2009](#)). Specifically, [Proctor et al. \(2009\)](#) found evidence of a rotating disk extending out to $\sim 1R_e$, while [Proctor et al. \(2005\)](#) found strong age and metallicity gradients within the inner $\sim 1R_e$ of the galaxy, with a young ($\sim 1-4$ Gyr old) and metal-rich ($[Z/H] \sim 0.5$ dex) central stellar population that transitions to an older (~ 10 Gyr) and more metal-poor ($[Z/H] \sim -0.5R_e$) one at $\sim 1R_e$.

The photometrically-identified GC system of NGC 821 contains 320 ± 45 objects and it displays a colour bimodality distribution at $(B - Rc) \sim 1.3$ ([Spitler et al. 2008](#)). This colour bimodality is also visible in the spectroscopic GC catalogue containing 68 objects. [Pota et al. \(2013\)](#) studied the kinematics of the two GC sub-populations separately in this galaxy, finding minor-axis rotation for the blue GCs, as was also observed for the PNe by [Coccato et al. \(2009\)](#). In this work, we choose not to split the GC population of NGC 821, as that would result in 14 red and 35 blue GCs, but we study the kinematics of the two GC sub-populations combined. In this way, we can work with a higher number of GCs to recover the kinematic profiles more reliably.

The PNe system contains 186 unique objects with measured radial velocities and it was obtained by combining the individual spectroscopic catalogues of [Coccato et al. \(2009\)](#) and [Teodorescu et al. \(2010\)](#). The former catalogue was observed as part of the ePN.S survey ([Pulsoni et al. 2018](#)) and contains 127 PNe, while the latter one was observed with the Subaru/FOCAS spectrograph and contains 155 PNe candidates (145 with measured radial velocities). We cross-match these PNe catalogues and find 84 objects in common in the two surveys, similarly to [Teodorescu et al. \(2010\)](#). The combination of the 84 common PNe with the 43 PNe from ePN.S and the 71 PNe from Subaru/FOCAS gives us a total of 188 PNe with measured radial velocities. After the removal of two objects from this sample that are outliers in the phase-space diagram, we end up with the final spectroscopic catalogue of 186 PNe with mean error on the radial velocity measurements of $\Delta V = 21$ km/s.

A2.1.1 Kinematic profiles

NGC 821 has a roughly flat stellar rotation velocity profile within $\sim 0.5R_e$ (from ATLAS^{3D}), which decreases out to $\sim 1R_e$ and, then, it remains roughly constant (from SLUGGS). The PNe show rotation between $\sim 1-2R_e$, followed by a subsequent decrease out to large radii, i.e. $\sim 4R_e$. The rotation velocity profile of the PNe is consistent with that of the stars at $\sim 1R_e$, however the PNe are rotating more closely aligned to the photometric minor-axis of the galaxy with $PA_{\text{kin}} \sim 150^\circ$ at all radii, while the stars show rotation along the galaxy photometric major-axis out to $\sim 1R_e$. A similar misalignment between the PA_{kin} of the PNe and the PA_{phot} of the galaxy was previously also found in [Coccato et al. \(2009\)](#). The GCs show decreasing rotation velocity profile out to $\sim 4R_e$, which is overall consistent with that of the PNe. The 2D kinematic maps in Fig. A5 show that also the GCs are rotating along a PA_{kin} which is misaligned from the PA_{phot} of the galaxy, similarly to the PNe. The derived 1D kinematic profile of the PA_{kin} of the GCs shows agreement with that of the stars (and, thus, with the PA_{phot} of the galaxy), however if we consider the large 1-sigma errors of the PA_{kin} profile of the GCs, then it is also consistent to some extent with the PA_{kin} profile of the PNe. [Pota et al. \(2013\)](#) found that the rotation along the photometric minor-axis of the galaxy is associated with the blue GC sub-population. Some GCs also show evidence of counter-rotation at $\sim 3R_e$ towards South-West (see Fig. A5).

The stellar velocity dispersion profile shows evidence of decreasing within $\sim 0.5R_e$ (ATLAS^{3D}) and, then, it is roughly constant at $\sim 140 \text{ km s}^{-1}$ at $\sim 1R_e$ (SLUGGS). The PNe show a decreasing velocity dispersion profile out to $\sim 1R_e$, consistent with both ATLAS^{3D} and SLUGGS. Beyond $\sim 1R_e$, the velocity dispersion profile of the PNe keeps decreasing out to $\sim 4R_e$. The GCs show a similar decreasing velocity dispersion profile, as the PNe, out to $\sim 4R_e$, as also shown by [Pota et al. \(2013\)](#).

The V_{rot}/σ profiles of the stars, PNe and GCs are very similar in shape to the corresponding rotation velocity profiles, with the stars showing decreasing V_{rot}/σ profiles out to $\sim 1R_e$ and the PNe and GCs out to $\sim 4R_e$.

The q_{kin} profile of the stars is consistent with the q_{phot} of the galaxy at $\sim 1R_e$, while it shows lower values within $\sim 0.5R_e$. The q_{kin} profile of the GCs agrees with that of the stars at $\sim 1R_e$, and, then, it smoothly decreases out to $\sim 4R_e$.

A2.2 NGC 4649

NGC 4649 (M60) is an elliptical galaxy of E2/S0 morphological type ([de Vaucouleurs et al. 1976](#)), belonging to the Virgo galaxy cluster. NGC 4649 is in a pair with the nearby smaller spiral galaxy, NGC 4647. However there are no clear signs of interactions between the two galaxies, whose optical light morphology does not look disturbed (e.g. [Pota et al. 2015](#)).

This is the galaxy with the largest GC system in our sample containing 431 objects. [Pota et al. \(2015\)](#) found evidence of a clear bimodal colour distribution of the GC population of NGC 4649 for $(g - z) = 1.2$, which we also adopt in this work, thus yielding 179 red, metal-rich and 252 blue, metal-poor GCs.

The PNe system contains 298 objects, which do not have complete coverage for position angles $280^\circ < PA < 310^\circ$ (with PA measured North towards East). The kinematic proper-

³ The NASA/IPAC Extragalactic Database (NED) is operated by the Jet Propulsion Laboratory, California Institute of Technology, under contract with the National Aeronautics and Space Administration.

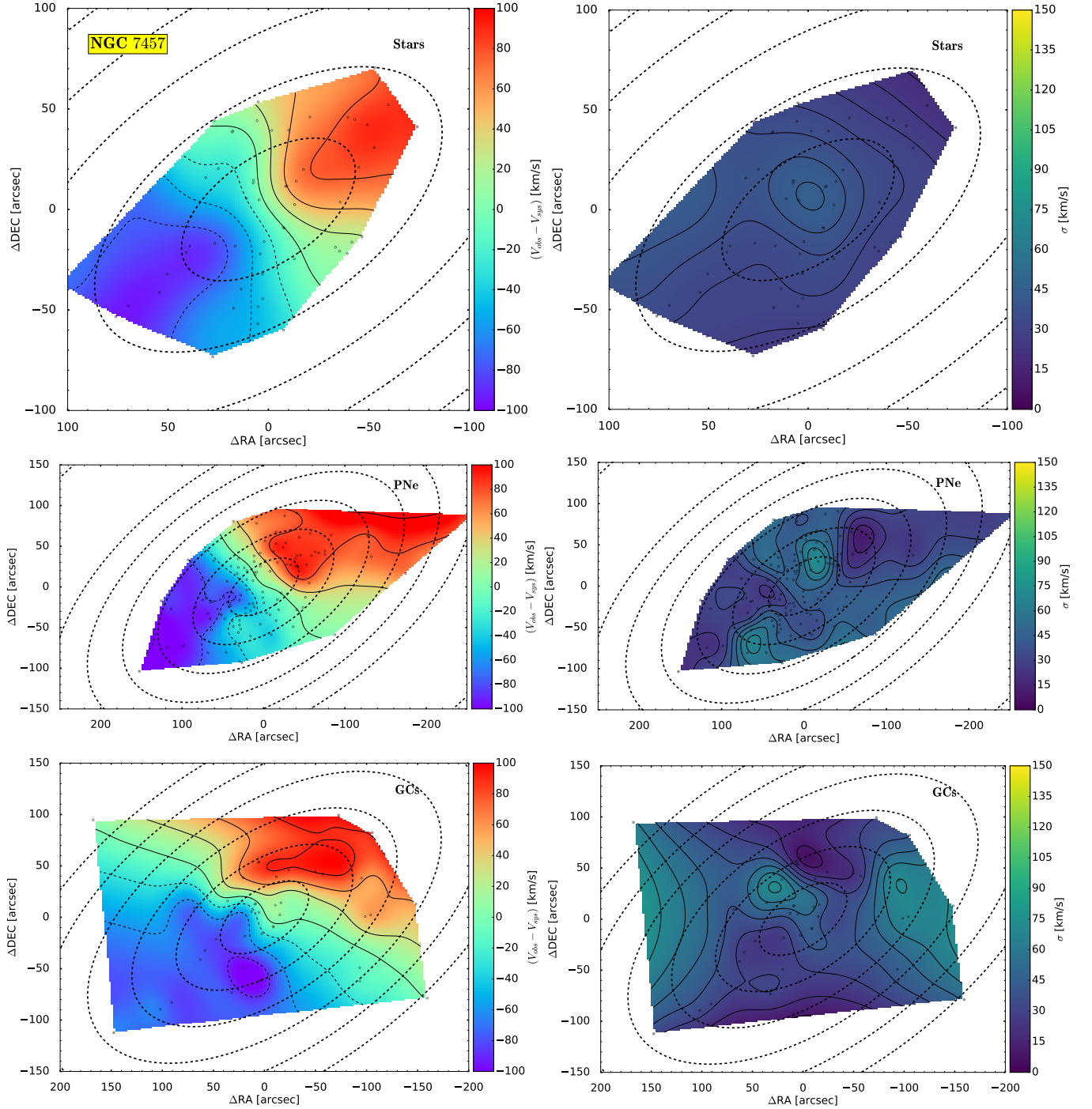


Figure A4. From top to bottom, 2D velocity (left-hand side) and velocity dispersion (right-hand side) maps of the SLUGGS stars, PNe and GCs for NGC 7457. The description is as in Fig. 2.

ties of the PNe were studied in [Coccato et al. \(2013\)](#), who found consistent rotation aligned with the stars along the galaxy photometric major-axis in the inner regions that becomes misaligned beyond $\sim 200''$.

Given the incomplete coverage for $280^\circ < \text{PA} < 310^\circ$, we test the symmetric properties of the PNe system with respect to the galaxy photometric axes and produce a denser distribution of tracers by *folding* the kinematic catalogue around its symmetry axis, similarly to NGC 3115 in [Dolfi et al. \(2020\)](#)

and to other galaxies in previous literature works (e.g. [Peng et al. 2004](#); [Cappellari et al. 2015](#); [Pulsoni et al. 2018](#)).

Before testing the point-symmetry of the PNe system of NGC 4649, we rotate the galaxy coordinates such that the photometric major-axis of the galaxy is aligned to the x -axis of an orthogonal reference system centred on NGC 4649. The new coordinates of this rotated system are calculated using equation 2 in [Dolfi et al. \(2020\)](#).

In the top panel of Fig. A6, we show the PNe veloci-

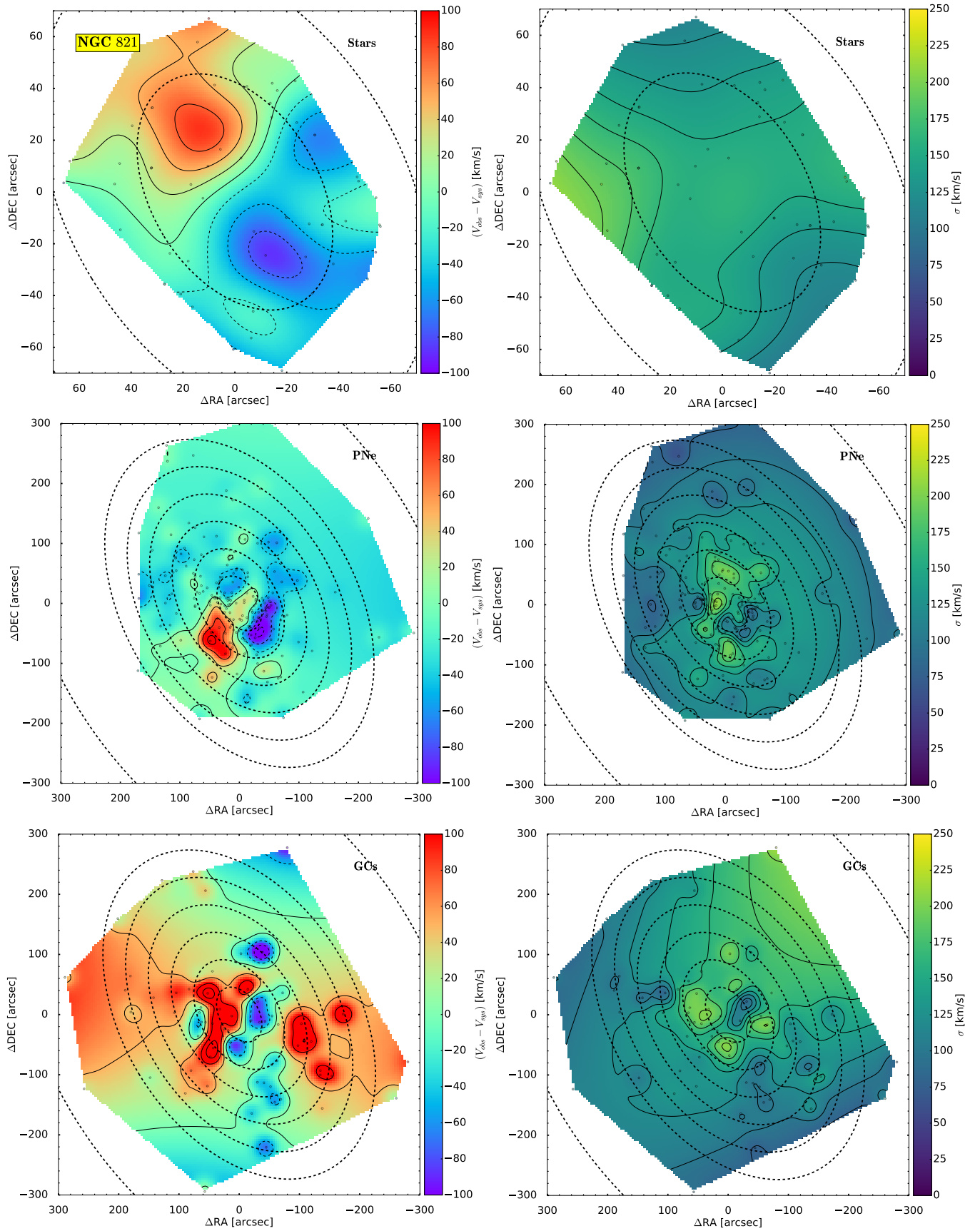


Figure A5. From top to bottom, 2D velocity (left-hand side) and velocity dispersion (right-hand side) maps of the SLUGGS stars, PNe and GCs for NGC 821. The description is as in Fig. 2.

ties, $V(R, \Phi)$, with $0^\circ < \Phi < 180^\circ$ (green points) and those, $-V(R, \Phi - 180^\circ)$, with $180^\circ < \Phi < 360^\circ$ (orange points) at all radii as a function of the position angle, Φ , of the tracers after subtracting the V_{sys} of NGC 4649. A significant overlap between the two velocity fields (i.e. $V(R, \Phi)$ and $-V(R, \Phi - 180^\circ)$) suggests that the system is symmetric with respect to the origin of the orthogonal reference system centred on NGC 4649.

Following Pulsoni et al. (2018), we fit our data with a rotation model function given by

$$V_{\text{obs}} = V_{\text{rot}} \cos(\phi - \text{PA}_{\text{kin}}) + s_3 \sin(3\phi - 3\text{PA}_{\text{kin}}) + c_3 \cos(3\phi - 3\text{PA}_{\text{kin}}), \quad (\text{A1})$$

where V_{rot} , PA_{kin} , s_3 and c_3 are the free parameters in the fit and ϕ is the independent x variable ranging between $[0, 180]^\circ$. In Eq. A1, the parameters s_3 and c_3 are the coefficients associated with higher order harmonics to account for deviations from the simple cosine law rotation model. As already done in Dolfi et al. (2020), and following Coccato et al. (2009), we assume the kinematic axial-ratio, $q_{\text{kin}} = 1$, in Eq. A1 for the purpose of testing the point-symmetry. The best-fit rotation model curve is represented by the black solid line in Fig. A6.

To quantify the degree of point-symmetry of the PNe system of NGC 4649, we calculate the difference of the PNe velocities from the best-fit model rotation function and we show the results in the form of normalized cumulative distribution functions for the PNe with $0^\circ < \Phi < 180^\circ$ (green line) and $180^\circ < \Phi < 360^\circ$ (orange line) as shown in the bottom panel of Fig A6. We find that the two functions are tracing the same underlying distribution with a probability $P_{\text{value}} = 87.3\%$ from the non-parametric two-sample Kolmogorow-Smirnow (KS) test. Therefore, the PNe system of NGC 4649 is point-symmetric (as previously found also in Coccato et al. 2013) and we can create the point-symmetric kinematic catalogue by taking the original catalogue and applying the following transformation $(X, Y, V) \rightarrow (-X, -Y, -V)$. The final PNe catalogue is twice as large as the original catalogue, being composed of the original catalogue and its point-symmetric counterpart.

A2.2.1 Kinematic profiles

NGC 4649 has a smoothly rising stellar rotation velocity profile out to $\sim 2.3R_e$. This is consistent with ATLAS^{3D} that shows rotation for the stars within $\sim 0.5R_e$. The rotation velocity profile of the PNe is consistent with that of the stars out to $\sim 1.5R_e$, where the PA_{kin} profiles of the stars and PNe show overall good kinematic alignment along the photometric major-axis of the galaxy. At $\sim 2R_e$, the rotation velocity of the PNe shows a dip in rotation. Beyond this radius, the rotation velocity of the PNe rises again and it is characterized by a new peak in rotation occurring beyond $\sim 2.5R_e$, where the PNe show rotation more closely aligned to the photometric minor-axis of the galaxy, as seen from the PA_{kin} profile. The red GCs show a similar double-peaked rotation velocity profile as the the PNe, with strong rotation ($\sim 350\text{km s}^{-1}$) within $\sim 1R_e$, where the PA_{kin} profile shows good kinematic alignment with both the stars and PNe, followed by a sharp drop in rotation out to $\sim 3R_e$. At larger radii, we see that the rotation velocity of the red GCs increases again and reaches a new peak in rotation between $\sim 5.6R_e$. The PA_{kin} profile of the red GCs does not show clear signs of kinematic twists as

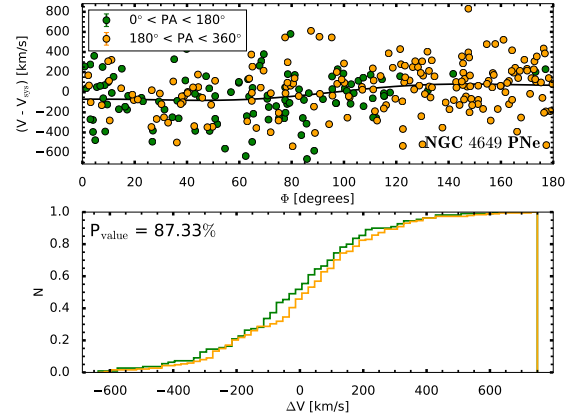


Figure A6. Point-symmetry for the PNe of NGC 4649. *Top panel:* velocities of the PNe as a function of their position angle, Φ . The PNe velocities on one side of the galaxy photometric major-axis (i.e. between $0^\circ < \text{PA} < 180^\circ$; green points) are compared with the velocities (changed in sign) on the opposite side (i.e. between $180^\circ < \text{PA} < 360^\circ$; orange points). The systemic velocity, V_{sys} , of the galaxy has been subtracted from the PNe velocities. The black solid line represents the best-fit model rotation curve from Eq. A1 fitted to the PNe velocities. *Bottom panel:* normalized cumulative distribution functions of the differences of the PNe velocities from the best-fit model rotation for the PNe with $0^\circ < \text{PA} < 180^\circ$ (green line) and with $180^\circ < \text{PA} < 360^\circ$ (yellow line). The P_{value} indicates the two-sample KS-test probability value for the null hypothesis that the two functions are tracing similar underlying distributions.

a function of galactocentric radius, suggesting that the rotation occurs along a similar kinematic axis at all radii. Pota et al. (2015) have also shown that the red GCs have overall constant PA_{kin} at all radii, consistent with the PA_{phot} of the galaxy. The blue GCs show a rotation velocity profile consistent with that of the stars between $\sim 1.2R_e$, beyond which it decreases out to large radii, i.e. $\sim 7R_e$. However, the blue GCs show rotation more closely aligned to the photometric minor-axis of the galaxy between $\sim 2.4R_e$, similarly to the PNe beyond $\sim 2.5R_e$, as was also previously found by Pota et al. (2015).

The velocity dispersion profile of the stars smoothly decreases out to $\sim 2.3R_e$, after the prominent central peak at $\sim 300\text{km s}^{-1}$, shown by ATLAS^{3D}. The velocity dispersion of the red GCs also shows a high central peak at $\sim 300\text{km s}^{-1}$ within $\sim 1.2R_e$, followed by a subsequent decrease out to $\sim 7R_e$, similarly to the stars (see Fig. A7) but with an offset of $\sim 50\text{km s}^{-1}$ to higher values. The PNe and blue GCs show similar velocity dispersion profiles out to $\sim 5.7R_e$, which are slightly decreasing along the photometric major-axis of the galaxy, while they remain roughly constant along the photometric minor-axis of the galaxy (see Fig. A7). The velocity dispersion of the PNe and blue GCs is also slightly higher than that of the red GCs beyond $\sim 2R_e$ (see Fig. 3).

The stellar V_{rot}/σ profile steeply rises out to $\sim 2R_e$, where it reaches its maximum value (i.e. $V_{\text{rot}}/\sigma \sim 1$). The blue GCs show a V_{rot}/σ profile consistent with the stars within $\sim 2R_e$, beyond which it decreases out to large radii (i.e. $\sim 7R_e$). The PNe and red GCs are characterized by a double-peaked V_{rot}/σ profile, with the first peak occurring at $\sim 1.15R_e$, where it is overall consistent with the stars. The second peak of the

V_{rot}/σ profile of the PNe and red GCs occurs at larger radii, i.e. $\sim 3R_e$ and $\sim 5-6R_e$, respectively, where the rotation is happening along the photometric minor-axis of the galaxy for the PNe. The dip in rotation velocity for the PNe and GCs was also previously found by Pota et al. (2015), who argued that it could be either not a real feature and due to the presence of the neighbouring spiral galaxy, NGC 4647, located between $\sim 2-3R_e$ towards North-West that prevents us from observing the GCs and PNe within that spatial region or it could be a result of the past interaction with the ultra-compact dwarf galaxy, UCD 1 (Strader et al. 2013).

A2.3 NGC 5846

NGC 5846 is a massive, bright early-type galaxy belonging to a galaxy group, which is located in the constellation Virgo. This galaxy has conflicting morphology, being classified as an E0-1 in RC2 and S0 in RSA (Michard & Marchal 1994). Early works have identified very little to no rotation from stellar (Emsellem et al. 2004; Foster et al. 2016) and GC kinematic (Pota et al. 2013) studies of this galaxy.

The GC system of NGC 5846 contains 215 objects. Pota et al. (2013) obtained photometry in the g , r and i bands for 195 GCs from their new Subaru observations and they identified a colour bi-modality distribution in the GC population for $(g-i) = 0.95$ mag. In this work, we adopt the same colour-split obtaining as final samples 103 red, metal-rich and 92 blue, metal-poor GCs.

The PNe system of NGC 5846 contains 124 objects and its kinematic properties were initially studied by Coccato et al. (2009), who did not find significant rotation along the major- and minor-axes.

A2.3.1 Kinematic profiles

NGC 5846 does not show any stellar rotation within $\sim 1-2R_e$, as previously shown by ATLAS^{3D} within $\sim 0.5R_e$. No net rotation is also seen for the PNe, whose rotation velocity profile is constant at $\sim 50\text{kms}^{-1}$ out to $\sim 5R_e$. The red GCs also show roughly constant rotation velocity profile out to $\sim 6R_e$, which is overall consistent with that of the PNe with a small offset in rotation. On the other hand, the blue GCs show rotation velocity, peaking at $\sim 200\text{kms}^{-1}$, between $\sim 1.5-2.5R_e$, which decreases out to large radii, i.e. $\sim 4R_e$, beyond which it is consistent with both that of the PNe and red GCs. However, from the 2D kinematic maps in Fig. A8, we do not see any clear evidence of rotation around the galaxy for the blue GCs. Pota et al. (2013) also found rotation for the blue GCs from the 1D kinematic profiles, but they argue that it may likely be due to few outliers GCs that belong to the nearby companion galaxy, NGC 5846A.

The stellar velocity dispersion is roughly constant at $\sim 200\text{kms}^{-1}$ within $\sim 1R_e$ and shows good agreement with the velocity dispersion profile of the PNe, which remains overall constant out to $\sim 5R_e$. The red and blue GCs also show velocity dispersion profiles, which are roughly constant out to $\sim 5R_e$ and overall consistent with the velocity dispersion profile of the PNe within the 1-sigma errors. However, the blue GCs show somewhat higher velocity dispersion than the red GCs and PNe (see Fig. A8).

The V_{rot}/σ profiles of the stars and PNe show that NGC 5846 has spheroid-like kinematics out to $\sim 5R_e$, with flat $V_{\text{rot}}/\sigma < 0.5$ at all radii. Similar behaviour is also observed

from the red and blue GCs V_{rot}/σ profiles, if the observed rotation between $\sim 1-2R_e$ (red GCs) and $\sim 1.5-2.5R_e$ (blue GCs) is, indeed, spurious and a consequence of outliers GCs. For this galaxy, we do not fit for the PA_{kin} and q_{kin} profiles of any kinematic dataset, as they are not well constrained from the **kinemetry** fit. However, we did calculate the 1D kinematic profiles for NGC 5846, leaving the PA_{kin} parameter free to vary for all our kinematic datasets, finding that both the rotation velocity and velocity dispersion profiles did not change significantly.

REFERENCES

- Arnold J. A., et al., 2014, *ApJ*, **791**, 80
 Barbon R., Capaccioli M., 1975, *A&A*, **42**, 103
 Bekki K., 1998, *ApJ*, **502**, L133
 Bekki K., 2009, *MNRAS*, **399**, 2221
 Bekki K., Couch W. J., 2011, *MNRAS*, **415**, 1783
 Bekki K., Beasley M. A., Brodie J. P., Forbes D. A., 2005, *MNRAS*, **363**, 1211
 Bellstedt S., Forbes D. A., Foster C., Romanowsky A. J., Brodie J. P., Pastorello N., Alabi A., Villaume A., 2017, *MNRAS*, **467**, 4540
 Blakeslee J. P., et al., 2009, *ApJ*, **694**, 556
 Boardman N. F., et al., 2017, *MNRAS*, **471**, 4005
 Bournaud F., Jog C. J., Combes F., 2005, *A&A*, **437**, 69
 Brodie J. P., Strader J., 2006, *ARA&A*, **44**, 193
 Brodie J. P., et al., 2014, *ApJ*, **796**, 52
 Bundy K., et al., 2015, *ApJ*, **798**, 7
 Buzzoni A., Arnaboldi M., Corradi R. L. M., 2006, *MNRAS*, **368**, 877
 Capaccioli M., Lorenz H., Afanasjev V. L., 1986, *A&A*, **169**, 54
 Cappellari M., et al., 2011, *MNRAS*, **413**, 813
 Cappellari M., et al., 2013, *MNRAS*, **432**, 1862
 Cappellari M., et al., 2015, *ApJ*, **804**, L21
 Cavanagh M. K., Bekki K., 2020, *A&A*, **641**, A77
 Ciardullo R., 2010, *Publ. Astron. Soc. Australia*, **27**, 149
 Coccato L., et al., 2009, *MNRAS*, **394**, 1249
 Coccato L., Arnaboldi M., Gerhard O., 2013, *MNRAS*, **436**, 1322
 Coccato L., et al., 2020, *MNRAS*, **492**, 2955
 Cook B. A., Conroy C., Pillepich A., Rodriguez-Gomez V., Hernquist L., 2016, *ApJ*, **833**, 158
 Corsini E. M., Morelli L., Pastorello N., Dalla Bontà E., Pizzella A., Portaluri E., 2016, *MNRAS*, **457**, 1198
 Cortesi A., et al., 2011, *MNRAS*, **414**, 642
 Cortesi A., et al., 2013a, *MNRAS*, **432**, 1010
 Cortesi A., et al., 2013b, *A&A*, **549**, A115
 Cortesi A., et al., 2016, *MNRAS*, **456**, 2611
 Croom S. M., et al., 2012, *MNRAS*, **421**, 872
 Damjanov I., Hwang H. S., Geller M. J., Chilingarian I., 2014, *ApJ*, **793**, 39
 Deeley S., et al., 2020, *MNRAS*, **498**, 2372
 Diaz J., Bekki K., Forbes D. A., Couch W. J., Drinkwater M. J., Deeley S., 2018, *MNRAS*, **477**, 2030
 Dolfi A., et al., 2020, *MNRAS*, **495**, 1321
 Domínguez Sánchez H., Bernardi M., Nikakhtar F., Margalef-Bentabol B., Sheth R. K., 2020, *MNRAS*, **495**, 2894
 Dressler A., 1980, *ApJ*, **236**, 351
 Dressler A., et al., 1997, *ApJ*, **490**, 577
 Drinkwater M. J., Jones J. B., Gregg M. D., Phillipps S., 2000, *Publ. Astron. Soc. Australia*, **17**, 227
 Eliche-Moral M. C., Rodríguez-Pérez C., Borlaff A., Querejeta M., Tapia T., 2018, *A&A*, **617**, A113
 Emsellem E., et al., 2004, *MNRAS*, **352**, 721
 Emsellem E., et al., 2011, *MNRAS*, **414**, 888

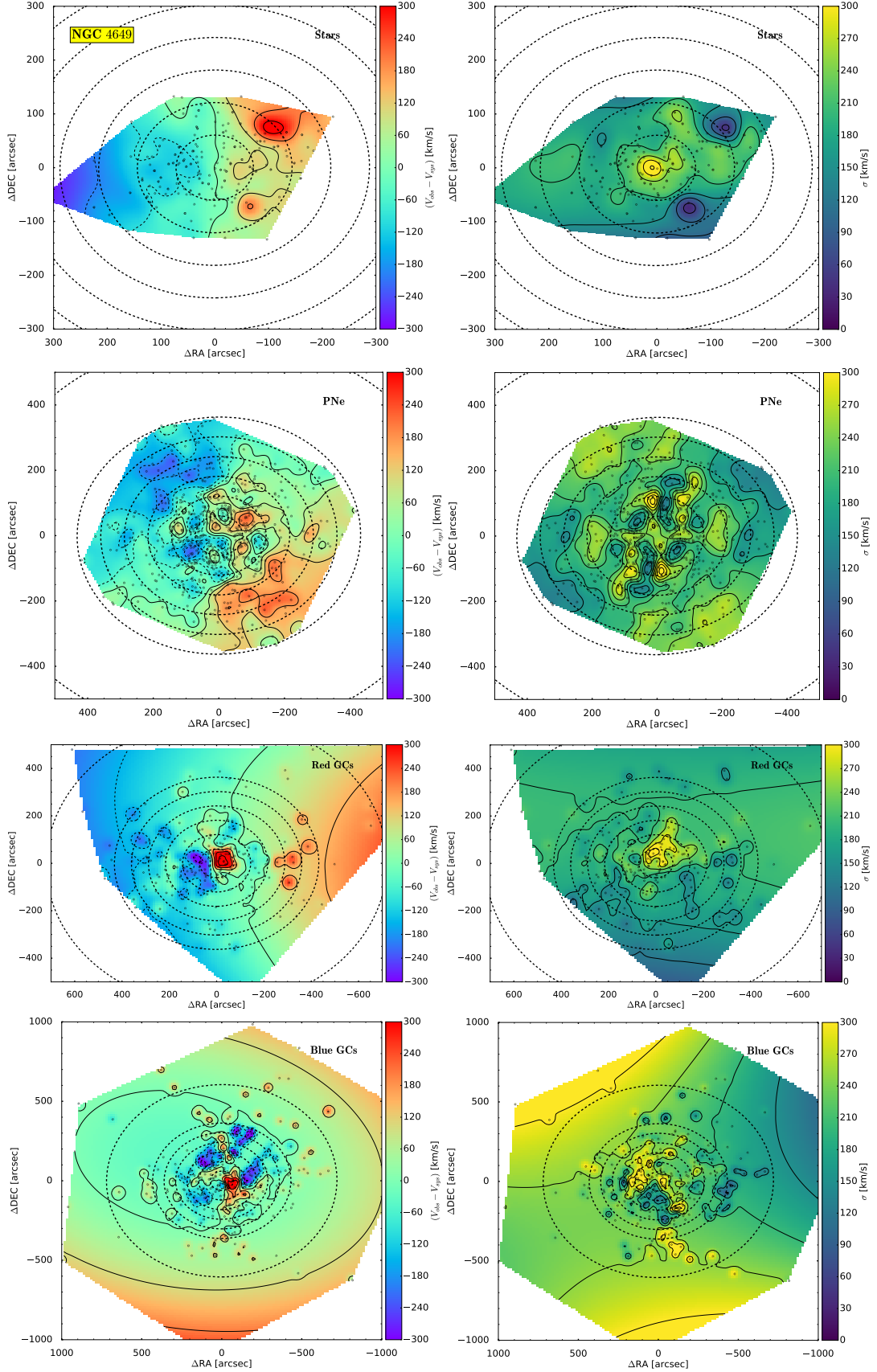


Figure A7. From top to bottom, 2D velocity (left-hand side) and velocity dispersion (right-hand side) maps of the SLUGGS stars, PNe, red and blue GCs for NGC 4649. The description is as in Fig. 2. We fold the PNe catalogue with respect to the galaxy centre (as described in Sec. A2.2) prior to producing the 2D kinematic maps, in order to account for the incomplete PA coverage of the PNe towards North-West (see Sec. A2.2). The description is as in Fig. 2.

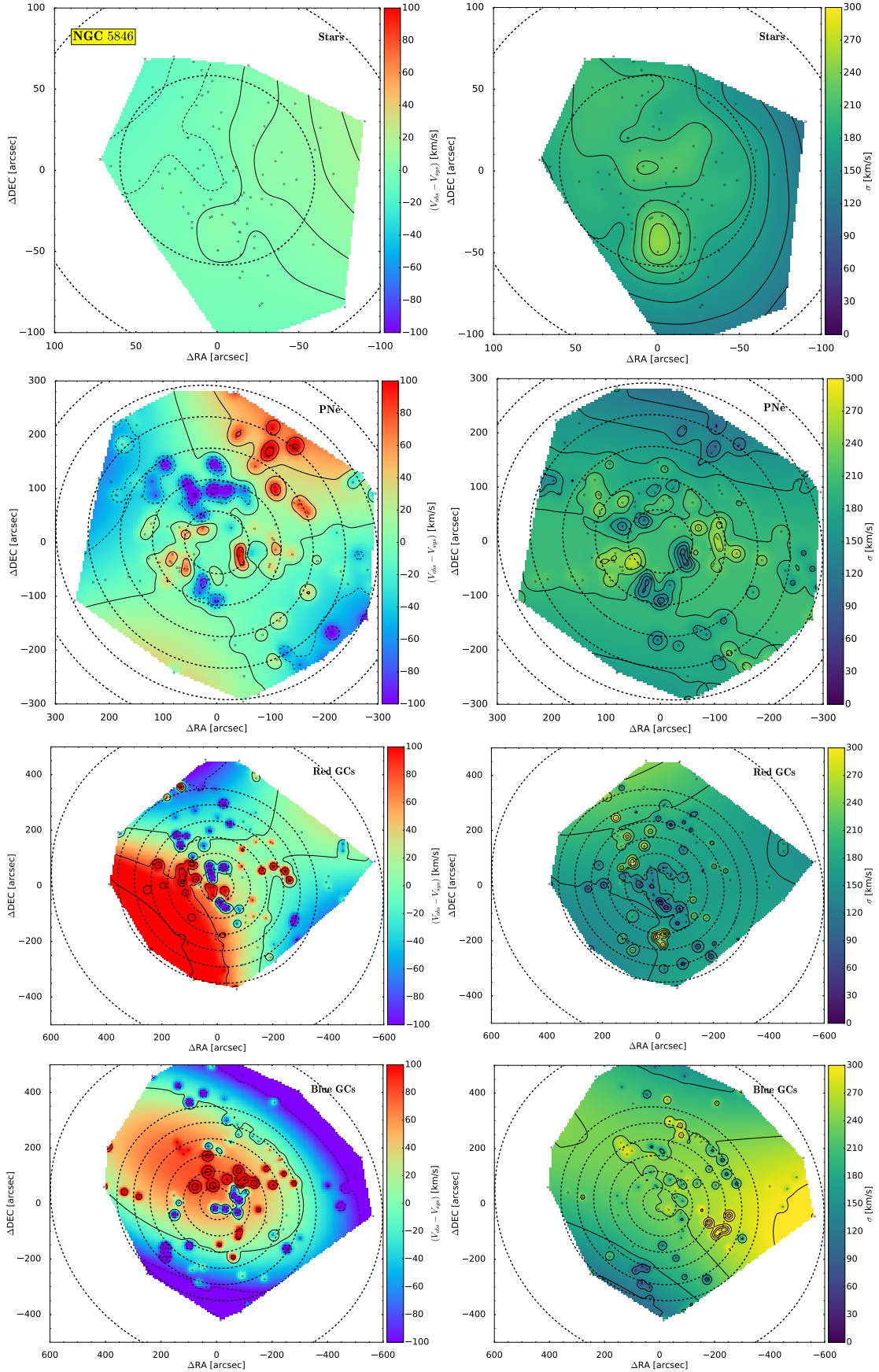


Figure A8. From top to bottom, 2D velocity (left-hand side) and velocity dispersion (right-hand side) maps of the SLUGGS stars, PNe, red and blue GCs of NGC 5846. The description is as in Fig. 2.

- Fasano G., Poggianti B. M., Couch W. J., Bettoni D., Kjærgaard P., Moles M., 2000, *ApJ*, **542**, 673
- Forbes D. A., Remus R.-S., 2018, *MNRAS*, **479**, 4760
- Forbes D. A., Brodie J. P., Grillmair C. J., 1997, *AJ*, **113**, 1652
- Forbes D. A., et al., 2012, *MNRAS*, **426**, 975
- Forbes D. A., et al., 2017a, *AJ*, **153**, 114
- Forbes D. A., Sinpetru L., Savorgnan G., Romanowsky A. J., Usher C., Brodie J., 2017b, *MNRAS*, **464**, 4611
- Ford H. A., Bregman J. N., 2013, *ApJ*, **770**, 137
- Foster C., Proctor R. N., Forbes D. A., Spolaor M., Hopkins P. F., Brodie J. P., 2009, *MNRAS*, **400**, 2135
- Foster C., et al., 2011, *MNRAS*, **415**, 3393
- Foster C., Arnold J. A., Forbes D. A., Pastorello N., Romanowsky A. J., Spitler L. R., Strader J., Brodie J. P., 2013, *MNRAS*, **435**, 3587
- Foster C., et al., 2016, *MNRAS*, **457**, 147
- Foster C., et al., 2018, *MNRAS*, **480**, 3105
- Fraser-McKelvie A., Aragón-Salamanca A., Merrifield M., Tabor M., Bernardi M., Drory N., Parikh T., Argudo-Fernández M., 2018, *MNRAS*, **481**, 5580
- Goudfrooij P., Hansen L., Jorgensen H. E., Norgaard-Nielsen H. U., de Jong T., van den Hoek L. B., 1994, *A&AS*, **104**, 179
- Guérou A., Emsellem E., Krajnović D., McDermid R. M., Contini T., Weilbacher P. M., 2016, *A&A*, **591**, A143
- Gunn J. E., Gott J. Richard I., 1972, *ApJ*, **176**, 1
- Halliday C., Davies R. L., Kuntschner H., Birkinshaw M., Bender R., Saglia R. P., Baggle G., 2001, *MNRAS*, **326**, 473
- Johnston E. J., et al., 2020, *MNRAS*,
- Kalirai J. S., Hansen B. M. S., Kelson D. D., Reitzel D. B., Rich R. M., Richer H. B., 2008, *ApJ*, **676**, 594
- Karademir G. S., Remus R.-S., Burkert A., Dolag K., Hoffmann T. L., Moster B. P., Steinwandel U. P., Zhang J., 2019, *MNRAS*, **487**, 318
- Kim D.-W., 1989, *ApJ*, **346**, 653
- Kormendy J., 1982, *ApJ*, **257**, 75
- Krajnović D., Cappellari M., de Zeeuw P. T., Copin Y., 2006, *MNRAS*, **366**, 787
- Krajnović D., et al., 2011, *MNRAS*, **414**, 2923
- Kroupa P., 2002, *Science*, **295**, 82
- Kuntschner H., et al., 2006, *MNRAS*, **369**, 497
- Kuntschner H., et al., 2010, *MNRAS*, **408**, 97
- Larson R. B., Tinsley B. M., Caldwell C. N., 1980, *ApJ*, **237**, 692
- Martig M., Bournaud F., Teyssier R., Dekel A., 2009, *ApJ*, **707**, 250
- McDermid R. M., et al., 2015, *MNRAS*, **448**, 3484
- Méndez R. H., Riffeser A., Kudritzki R. P., Matthias M., Freeman K. C., Arnaboldi M., Capaccioli M., Gerhard O. E., 2001, *ApJ*, **563**, 135
- Méndez R. H., Teodorescu A. M., Kudritzki R. P., 2008, *ApJS*, **175**, 522
- Merluzzi P., Busarello G., Dopita M. A., Haines C. P., Steinhauser D., Bourdin H., Mazzotta P., 2016, *MNRAS*, **460**, 3345
- Michard R., Marchal J., 1994, *A&AS*, **105**, 481
- Mishra P. K., Wadadekar Y., Barway S., 2018, *MNRAS*, **478**, 351
- Naab T., et al., 2014, *MNRAS*, **444**, 3357
- Noordermeer E., et al., 2008, *MNRAS*, **384**, 943
- Oser L., Ostriker J. P., Naab T., Johansson P. H., Burkert A., 2010, *ApJ*, **725**, 2312
- Pastorello N., Forbes D. A., Foster C., Brodie J. P., Usher C., Romanowsky A. J., Strader J., Arnold J. A., 2014, *MNRAS*, **442**, 1003
- Peng E. W., Ford H. C., Freeman K. C., 2004, *ApJ*, **602**, 685
- Poci A., McDermid R. M., Zhu L., van de Ven G., 2019, *MNRAS*, **487**, 3776
- Pota V., et al., 2013, *MNRAS*, **428**, 389
- Pota V., et al., 2015, *MNRAS*, **450**, 1962
- Proctor R. N., Forbes D. A., Forestell A., Gebhardt K., 2005, *MNRAS*, **362**, 857
- Proctor R. N., Forbes D. A., Romanowsky A. J., Brodie J. P., Strader J., Spolaor M., Mendel J. T., Spitler L., 2009, *MNRAS*, **398**, 91
- Pulsoni C., et al., 2018, *A&A*, **618**, A94
- Pulsoni C., Gerhard O., Arnaboldi M., Pillepich A., Rodriguez-Gomez V., Nelson D., Hernquist L., Springel V., 2020, arXiv e-prints, p. [arXiv:2009.01823](https://arxiv.org/abs/2009.01823)
- Raskutti S., Greene J. E., Murphy J. D., 2014, *ApJ*, **786**, 23
- Ravindranath S., Ho L. C., Peng C. Y., Filippenko A. V., Sargent W. L. W., 2001, *AJ*, **122**, 653
- Rizzo F., Fraternali F., Iorio G., 2018, *MNRAS*, **476**, 2137
- Rodriguez-Gomez V., et al., 2016, *MNRAS*, **458**, 2371
- Romanowsky A. J., 2006, in Barlow M. J., Méndez R. H., eds, Vol. 234, *Planetary Nebulae in our Galaxy and Beyond*. pp 341–348 ([arXiv:astro-ph/0605275](https://arxiv.org/abs/astro-ph/0605275)), doi:10.1017/S174392130600319X
- Saha K., Cortesi A., 2018, *ApJ*, **862**, L12
- Sambhus N., de Lorenzi F., Gerhard O., 2006, in Stanghellini L., Walsh J. R., Douglas N. G., eds, *Planetary Nebulae Beyond the Milky Way*. p. 318, doi:10.1007/3-540-34270-2_50
- Sancisi R., van Woerden H., Davies R. D., Hart L., 1984, *MNRAS*, **210**, 497
- Sandage A., Bedke J., 1994, *The Carnegie atlas of galaxies*. Vol. 638
- Sandage A., Tammann G. A., 1987, *A Revised Shapley-Ames Catalog of Bright Galaxies*
- Sarzi M., et al., 2006, *MNRAS*, **366**, 1151
- Schulze F., Remus R.-S., Dolag K., Bellstedt S., Burkert A., Forbes D. A., 2020, *MNRAS*, **493**, 3778
- Sil'chenko O. K., Afanasiev V. L., Chavushyan V. H., Valdes J. R., 2002, *ApJ*, **577**, 668
- Spiniello C., Napolitano N. R., Coccato L., Pota V., Romanowsky A. J., Tortora C., Covone G., Capaccioli M., 2015, *MNRAS*, **452**, 99
- Spitler L. R., Forbes D. A., Strader J., Brodie J. P., Gallagher J. S., 2008, *MNRAS*, **385**, 361
- Strader J., Brodie J. P., Forbes D. A., 2004, *AJ*, **127**, 3431
- Strader J., Brodie J. P., Cenarro A. J., Beasley M. A., Forbes D. A., 2005, *AJ*, **130**, 1315
- Strader J., et al., 2013, *ApJ*, **775**, L6
- Tapia T., Eliche-Moral M. C., Aceves H., Rodríguez-Pérez C., Borlaff A., Querejeta M., 2017, *A&A*, **604**, A105
- Teodorescu A. M., Méndez R. H., Bernardi F., Riffeser A., Kudritzki R. P., 2010, *ApJ*, **721**, 369
- Tous J. L., Solanes J. M., Perea J. D., 2020, *MNRAS*, **495**, 4135
- Tully R. B., 1980, *ApJ*, **237**, 390
- Usher C., Brodie J. P., Forbes D. A., Romanowsky A. J., Strader J., Pfeffer J., Bastian N., 2019, *MNRAS*, **490**, 491
- Wiklund T., Henkel C., 1995, *A&A*, **297**, L71
- Zanatta E. J. B., et al., 2018, *MNRAS*, **479**, 5124
- Zolotov A., et al., 2015, *MNRAS*, **450**, 2327
- de Vaucouleurs G., de Vaucouleurs A., Corwin J. R., 1976, *Second reference catalogue of bright galaxies*, 1976, 0

This paper has been typeset from a \LaTeX file prepared by the author.